DR. 772

GA-A15564
UC-77

173
3/3/80

MASTER

INFLUENCE OF A SIMULATED HTGR ENVIRONMENT ON THE MECHANICAL PROPERTIES OF A COMMERCIAL Ni-Cr-Mo-Fe ALLOY (HASTELLOY ALLOY X)

by
C. C. LI, W. R. JOHNSON, and L. D. THOMPSON

Prepared under
Contract DE-AT03-76ET35300
for the San Francisco Operations Office
Department of Energy

DATE PUBLISHED: DECEMBER 1979

GENERAL ATOMIC COMPANY

DISCLAIMER

NOTICE

Printed in the United States of America
Available from
National Technical Information Service
U.S. Department of Commerce
5285 Port Royal Road
Springfield, Virginia 22161
Price: Printed Copy $5.25; Microfiche $3.00

GA-A15564
UC-77

INFLUENCE OF A SIMULATED HTGR ENVIRONMENT ON THE MECHANICAL PROPERTIES OF A COMMERCIAL Ni-Cr-Mo-Fe ALLOY (HASTELLOY ALLOY X)

by
C. C. LI, W. R. JOHNSON, and L. D. THOMPSON

Prepared under
Contract DE-AT03-76ET35300
for the San Francisco Operations Office
Department of Energy

GENERAL ATOMIC PROJECT 6400
DATE PUBLISHED: DECEMBER 1979

GENERAL ATOMIC COMPANY

THIS PAGE

WAS INTENTIONALLY

LEFT BLANK

ABSTRACT

The influence of a simulated advanced-reactor helium environment, containing 500 μatm H_2/50 μatm CH_4/50 μatm CO/~1 μatm H_2O, on the mechanical properties of two heats of Hastelloy Alloy X is discussed. Simultaneous exposures in air and controlled-impurity helium at temperatures in the range of 650° to 1000°C for times of 3000 h or more were performed. A combination of tensile testing, Charpy V-notch impact toughness testing, and creep testing was used to study the effects of reactor helium/metal interactions on the mechanical behavior of this alloy.

Carburization was identified as the primary corrosion phenomenon. Increasing exposure time and temperature were observed to increase the depth of carburization. The increase in carbon concentration in the carburized zone suppressed the additional formation of M_6C, which is observed in air-aged specimens, and resulted in the precipitation of $M_{23}C_6$, a chromium-rich carbide variant. The precipitation of $M_{23}C_6$ in the carburized zone occurred primarily along grain and twin boundaries; however, matrix precipitation was also observed, the degree of which depended on exposure temperature.

Strength and impact toughness properties were found to be controlled primarily by thermal aging reactions, with only a small effect related to the carburization. Although tensile and creep ductilities were decreased as a result of carburization, substantial ductility remained. Variation was observed between the two heats, the finer-grained heat appearing to be weaker in the high-temperature creep tests and also possibly more susceptible to a loss of creep strength as a result of carburization.

THIS PAGE

WAS INTENTIONALLY

LEFT BLANK

CONTENTS

FIGURES

FIGURES (continued)

FIGURES (continued)

TABLES

1. INTRODUCTION

Hastelloy Alloy X* is being considered as one of the major high-temperature alloys for structural component applications in an advanced-design, gas-turbine high-temperature gas-cooled reactor (GT-HTGR). This alloy is currently being employed in an operating steam-cycle HTGR designed and constructed by General Atomic Company (GA). The steam-cycle HTGR is a uranium-thorium-fueled, graphite-moderated reactor system in which the fission heat generated in the reactor core is transferred by high-pressure helium coolant gas to steam generators where superheated steam is produced for electric power generation. In the direct-cycle GT-HTGR currently under design, the helium coolant is transferred directly to a gas turbine for power conversion, thus circumventing the need for intermediate heat exchangers or steam generators.

Materials selection for many of the plant (non-core) components of these reactors is strongly influenced by the high temperatures and long life (40 years) required by the reactor design. Thus, it is necessary to develop a high degree of understanding concerning the long-time thermal response of alloy structures and subsequent effects on mechanical properties.

The chemical inertness of the helium primary coolant gas allows the HTGR system to take advantage of the excellent elevated temperature properties of a material such as graphite. However, although helium is inert, there are practical limits to the primary coolant purity levels obtainable in an actual operating HTGR. The unavoidable presence of small quantities of impurities in the helium coolant requires that an understanding of the interaction of structural materials with these impurities be obtained.

---

*Hastelloy Alloy X is a registered trademark of Cabot Corporation. Material of the same specified composition supplied by other producers is normally identified as Alloy X.

The principal HTGR primary coolant impurities which are potentially important with respect to materials compatibility include H_2, H_2O, CO, CO_2, and CH_4. These impurities may arise from a variety of sources, such as steam ingress and proton diffusion through steam tubes (in steam cycle systems), outgassing of reactor components, oil ingress, and reaction of these primary source impurities with the core graphite.

The potential interaction of structural metals with primary coolant impurities is of prime concern in reactor design since degradation of properties may result from gas/metal reactions such as internal oxidation or interstitial transport (carburization or decarburization, for example). Recent experiments such as those on the long-term exposure of several component materials to a simulated GT-HTGR helium environment have shown significant carburization of both wrought and cast alloys (Refs. 1-3). Extensive experimental programs are currently in progress at GA to investigate the HTGR helium corrosion behavior and its influence on the mechanical properties of candidate alloys. This paper reports the experimental results of 3000-h tests of Hastelloy X exposed to a simulated GT-HTGR environment and to air at temperatures from 650° to 1000°C.

2. EXPERIMENTAL PROCEDURES

Two alloy heats, obtained from different vendors, were employed in this study. In this and subsequent sections of this report, both heats are referred to as Hastelloy X for convenience. Both alloys were received in the form of 12.7 mm (0.5 in.) diameter bars. The two heats, identified herein as 081 and 086, were solution annealed at 1177°C (2150°F) for 20 and 45 min, respectively, and then water quenched. The grain size and chemical composition of the two heats are listed in Table 1.

Tensile and creep specimens, 6.35 mm (0.250 in.) diameter x 31.75 mm (1.25 in.) gage length, and ASTM standard Charpy V-notch impact specimens, 55.0 mm (2.165 in.) x 10.0 mm (0.394 in.) x 10.0 mm (0.394 in.), were machined from the solution-annealed bars. Specimens were then isothermally exposed unstressed and/or stressed in creep for 3000 h at 650°, 800°, 900°, and 1000°C in a simulated GT-HTGR helium environment containing controlled amounts of H_2, CH_4, CO, and H_2O. Companion tensile, creep, and impact specimens were exposed/stressed in air for one or both heats at 650° (creep only), 800°, 900°, and 1000°C (creep only).

2.1. ENVIRONMENTAL EXPOSURES

The creep tests were conducted at the Central Institute for Industrial Research (CIIR) in Oslo, Norway, using an uninstrumented, multiple-specimen string technique in which the creep tests are interrupted and creep strains are measured on unloaded specimens initially at 500-h and thereafter at 1000-h intervals. The stress levels employed, shown in Table 2, were selected for each temperature to approximate two-thirds the estimated stress-for-rupture in 100,000 to 200,000 h, based on vendor air data.

The controlled-impurity helium exposure system utilized for the creep tests at CIIR has been fully described in Ref. 1. The system is divided

TABLE 1
GRAIN SIZE AND CHEMICAL COMPOSITION OF HASTELLOY X
(SOLUTION-ANNEALED)

	Heat 081	Heat 086
Average grain size, mm	0.090	0.160
ASTM No.	3-5	2-4
Chemical composition, wt %		
Carbon	0.092	0.080
Manganese	0.58	0.48
Silicon	0.96	0.49
Phosphorus	0.018	0.023
Sulfur	0.005	0.005
Boron	0.003	<0.002
Nickel	46.7	45.3
Chromium	21.9	20.5
Molybdenum	9.0	8.6
Cobalt	1.65	2.1
Tungsten	0.44	0.5
Iron	17.9	20.9
Aluminum	<0.10	<0.10
Titanium	<0.10	<0.10
Copper	0.05	0.20
Vanadium	<0.10	<0.10
Niobium	<0.10	0.25
Tantalum	<0.10	<0.10
Yttrium	<0.10	<0.10
Zirconium	0.03	<0.10

TABLE 2
SUMMARY OF RESULTS OF CARBURIZATION DEPTH AND BULK CARBON CONTENT MEASUREMENTS FOR HELIUM-EXPOSED HASTELLOY X

Specimen No.[a]	Type of Specimen	Exposure Temp (°C)	Stress Applied During Exposure (MPa)	Bulk Carbon Content (wt %)	Relative Percentage Carbon Increase	Carburized Depth (μm)[b]
08182	Impact	800	--	0.12	30.4	114
08683	Impact	800	--	0.097	21.3	167
08684	Impact	800	--	0.095	18.8	122
08184	Impact	900	--	0.16	73.9	232
08115	Tensile	800	--	0.11	19.6	105
08116	Tensile	800	--	0.11	19.6	77
08607	Tensile	800	--	0.097	21.4	109
08125	Tensile	900	--	0.17	84.8	267
08126	Tensile	900	--	0.16	73.9	284
08602	Tensile	900	--	0.13	62.5	236
08604	Tensile	900	--	0.18	125	592
08105	Creep	650	103	0.10	8.7	0
08605	Creep	800	31	0.11	37.5	273[c] (325)[d]
08104	Creep[e]	900	12.8	--	--	281[c] (267)[d]
08609	Creep	900	12.8	0.15	87.5	513[c] (498)[d]
08611	Creep	1000	4.8	0.16	100	1123[c] (738)[d]

[a]The first three digits of the specimen number refer to the heat number.
[b]Depth of carburization is determined by the DIC method.
[c]Measured in stressed area (gage section).
[d]Measured in unstressed area (shoulder section).
[e]Ruptured after 3170 h.

into a gas loop, which provides the test helium at prescribed controlled-impurity levels, and a furnace loop, which receives the controlled-impurity helium and exposes specimens under controlled temperatures and loading conditions. The gas circuit consists of two main parts, a purification loop and a helium loop with a large manifold supplying gas to the test furnaces. In the purification loop, commercially pure helium is purified to very low partial pressures of the impurities CO, CO_2, H_2, H_2O, O_2, and N_2. The H_2, CO, and H_2O content of the controlled-impurity test helium is regulated by varying the amount of H_2O injected into the loop as well as the temperature and gas flow through a graphite furnace, where H_2O is converted to CO and H_2. Methane (CH_4) is injected into the loop independently. The helium flow rate in each furnace is maintained at 1000 cc/min. The instrument circuit monitors and controls the impurity content of the test gas. Hydrogen is monitored by converting it to H_2O in a CuO furnace and employing a P_2O_5 Meeco Model W electrolytic H_2O analyzer (to 10 μatm). Water is monitored with a Goldsmith P_2O_5 cell with extra-fine platinum electrodes. A detection limit of 0.2 ± 0.04 μatm H_2O is obtained. The overall loop and the outlet gases from each set of furnaces are monitored. A Carle Model 8000 gas chromatograph monitors CH_4 and CO.

The helium impurity histograms for the first 3000 h of creep testing at CIIR are shown in Fig. 1. The levels of CH_4 and CO were initially lower than the target values of 50 μatm. By the end of 3000 h, the CH_4 partial pressure was brought up to 50 μatm but the CO partial pressure could not be increased much above 30 μatm. The H_2 and H_2O partial pressures were at or near the target values of 500 μatm and 1.5 μatm, respectively, during the first 3000 h of testing. For test exposure times greater than 3000 h, impurity levels were maintained within ±20% of the values established after 3000 h of exposure.

The unstressed aging tests on tensile and impact specimens were conducted at GA for temperatures of 800° and 900°C employing the same alloy heats and nominal helium impurity levels as those at CIIR. Unlike

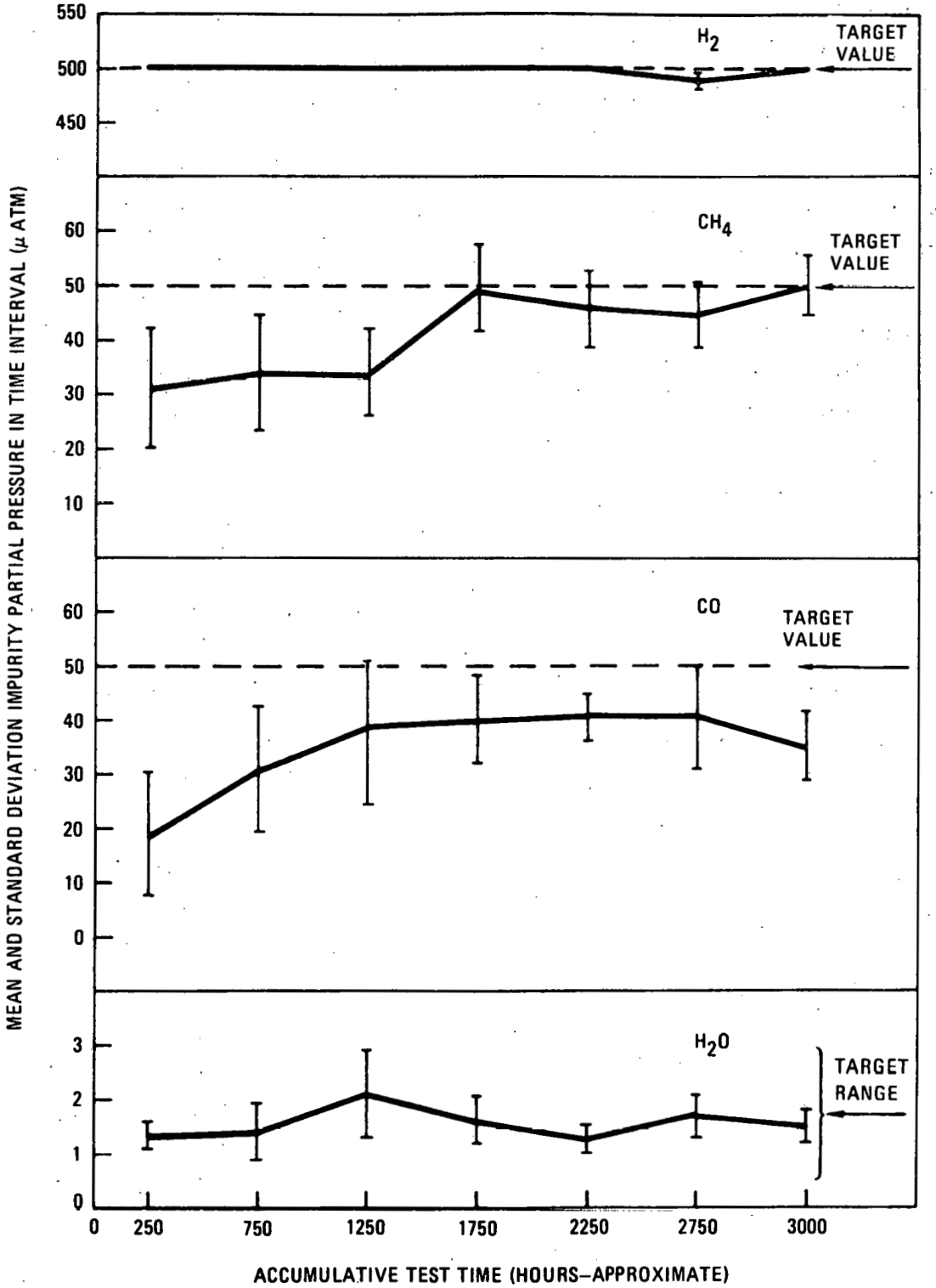

Fig. 1. Impurity histograms for CIIR controlled-impurity helium loop during first 3000 h of creep screening tests

the controlled-impurity helium loop utilized at CIIR, a once-through system was employed at GA. This system has also been fully described (Ref. 1). In this system, the controlled-impurity helium environment is prepared by first purifying commercial atomic-grade helium (99.995% purity) by passing the gas through a 5 Å molecular sieve/activated charcoal trap maintained at liquid nitrogen temperature (-196°C). Controlled quantities of research-purity H_2, CH_4, and CO are added through special micrometering vacuum valves to a mixing manifold, and the mixture is supplied to the aging furnace retort at 470 cc/min and 1.05 atm pressure. No H_2O is deliberately introduced into the controlled-impurity helium. The H_2, CO, and CH_4 concentrations in the helium are measured using a Carle Model 111H gas chromatograph, while an EG&G Model 440 hygrometer with auxiliary cooling and extended range capabilities is employed to continuously monitor moisture levels.

The helium impurity histograms representative of the conditions for the GA once-through system during the 3000-h exposures are shown in Fig. 2. The H_2O levels were below 1 μatm (the detection limit of the hygrometer) throughout most of the test period and were somewhat lower than the 1.5 μatm maintained for the creep tests at CIIR. The CH_4 and CO partial pressures were within ~10% of the 50 μatm target value during most of the 3000-h test time. The H_2 level was consistently within ~10% during the total test interval.

2.2. MECHANICAL PROPERTY AND METALLURGICAL EVALUATIONS

After 3000 h of exposure, tensile and impact specimens exposed in helium and air at GA, and selected creep specimens exposed in helium and air at CIIR, were removed and subsequently fractured in tension or impact at room temperature. Tension tests were conducted at GA using an MTS (Materials Testing Systems) universal test machine employing a constant loading rate of 2.22×10^5 N/min (5000 lb/min). Impact tests were conducted using an instrumented Tinius-Olsen impact machine. Several creep specimens of one of the Hastelloy X heats (heat 081) ruptured prior to

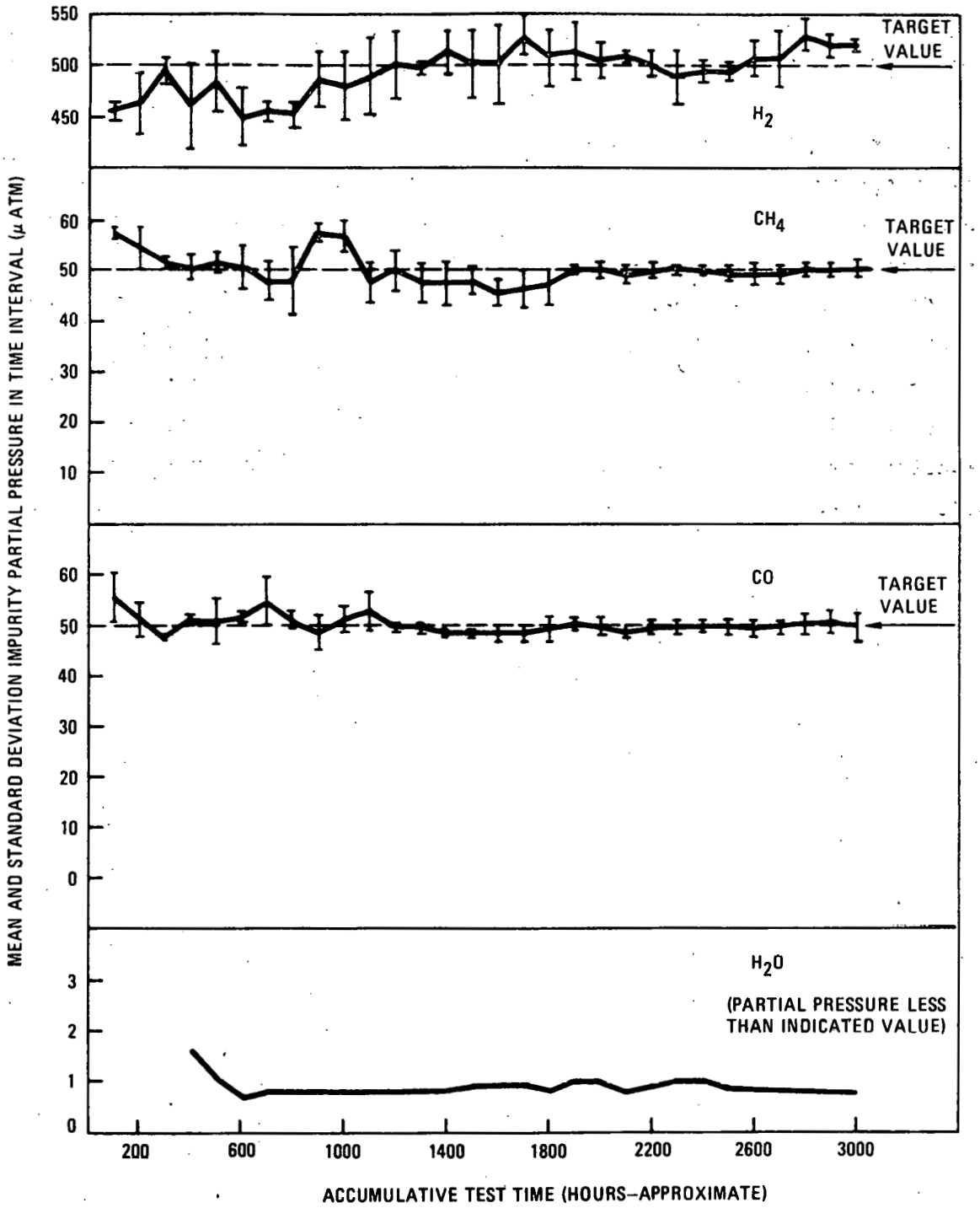

Fig. 2. Impurity histograms for GA once-through controlled-impurity helium supply system during first 3000 h of unstressed aging tests

reaching 3000 h of testing; therefore, no tensile data were obtained from these specimens. A number of helium and air creep tests for both heats are being continued at CIIR.

Fractured specimens were subjected to detailed metallurgical analyses including optical and scanning electron microscopy (SEM), SEM energy dispersive x-ray (EDX) analysis, bulk carbon content determination, and x-ray diffraction phase analysis. Carburization, where observed, was measured by a differential interference contrast method using an optical microscope with polarized light. Electrolytic surface extractions of precipitated phases and surface scales from selected specimens were conducted at room temperature using an electrolyte containing 10% HCl in methanol. X-ray diffraction analyses of extractions were performed using a Nonius Guinier de Wolff quadrupole-focusing camera in conjunction with Cu Kα radiation.

3. RESULTS

3.1. CREEP TESTS

The controlled-impurity helium and air creep test results for both heats of Hastelloy X are summarized in Table 3. Data from tests at 650°, 800°, 900°, and 1000°C are shown. The table indicates the total creep strain at 1000-h intervals (or 5000-h intervals after 10,000 h of testing) for all continuing and terminated tests, and final creep strains for specimens that ruptured during testing.

Plots comparing creep strain as a function of time in controlled-impurity helium and in air for one or both heats are shown in Fig. 3 at 650°C, Fig. 4 at 800°C, Figs. 5 and 6 at 900°C, and Fig. 7 at 1000°C. Comparison of the creep curves in controlled-impurity helium and air at 650°, 800°, and 900°C indicates similar creep behavior in both environments at these three temperatures. It should be mentioned that the inherent scatter in creep testing, particularly in comparing data from single specimens, has shown that differences in creep strains on the order of several tenths of a percent are probably not significant at these relatively low stresses, where scatter is amplified, especially during the early (primary and secondary) stages of high-temperature creep. Within experimental scatter, therefore, the creep behavior of Hastelloy X at 650° and 800°C and of heat 086 at 900°C appears to be similar in helium and air, the maximum difference in creep strain between air- and helium-tested specimens at any temperature being less than ~0.4%.

Comparison of the helium and air creep curves for heat 081 at 900°C indicates what appear to be significant differences in creep behavior between two of the helium-tested specimens and the air-tested specimen, while one helium-tested specimen exhibited creep behavior nearly identical

TABLE 3
COMPARISON OF CREEP DATA FOR HASTELLOY X EXPOSED IN CONTROLLED-IMPURITY HELIUM AND AIR

Heat No.	Exposure Temp (°C)	Exposure Environment	Applied Stress (MPa)	Strain Measured After Exposure (%)														
				500 H	1000 H	1500 H	2000 H	2500 H	3000 H	4000 H	5000 H	6000 H	7000 H	8000 H	9000 H	10,000 H	15,000 H	20,000 H
081	650	Air	105.4	0.18	0.29		0.40		0.40									
081	650	He	106.3	0.01	--	0.10	0.21	--	0.22									
081	650	He	106.0	0.26	--	0.26	--	--	--	0.49	0.57	0.57	0.58	0.60	0.64	0.64	0.69	0.73
081	800	Air	31.8	--	--	--	0.14	--	0.14	0.17	0.17	0.17	0.21	0.21	0.28	0.23	0.27	0.36
086	800	Air	32.0	0.16	0.21	--	0.22	--	0.24	0.24	0.23	0.26	0.25	0.36	0.36	0.36	0.39	
081	800	He	31.9	0.00	--	--	0.00	--	0.07	0.07	0.07	0.07	0.07	0.14	0.17	0.19	0.51	0.67
086	800	He	31.9	0.16	0.17	--	0.17	--	0.15	0.18	0.23	0.38	0.39	0.43	0.42	0.47	--	--
081	900	Air	13.0	0.00	0.00	--	0.60	--	1.10	1.94	2.97	5.60	14.05	(Ruptured at 7945 h at 22.82%)				
086	900	Air	13.0	0.06	0.22	--	0.24	--	0.36	0.41	0.58	0.61	--	0.81	1.16	1.68		
081	900	He	13.0	0.02	0.19		1.51	(Ruptured at 2760 h at 5.02%)										
081	900	He	13.0	0.02	0.10		0.82		2.85	(Ruptured at 3170 h at 4.85%)								
081	900	He	13.0	0.00	0.06		0.33		0.36	2.02	2.40	(Ruptured at 5290 h at 4.40%)						
086	900	He	13.1	0.02	0.07		0.22		0.41	(Terminated)								
086	900	He	13.0	0.12	0.18		0.26		0.36	0.41	0.59	0.70	0.77	0.90	0.96	1.13		
086	1000	He	4.9	0.02	0.18		0.57	(Terminated)										
086	1000	He	4.8	0.10	0.18		0.33		1.87	1.93	2.23	2.37	2.49	3.72	4.61	4.73		

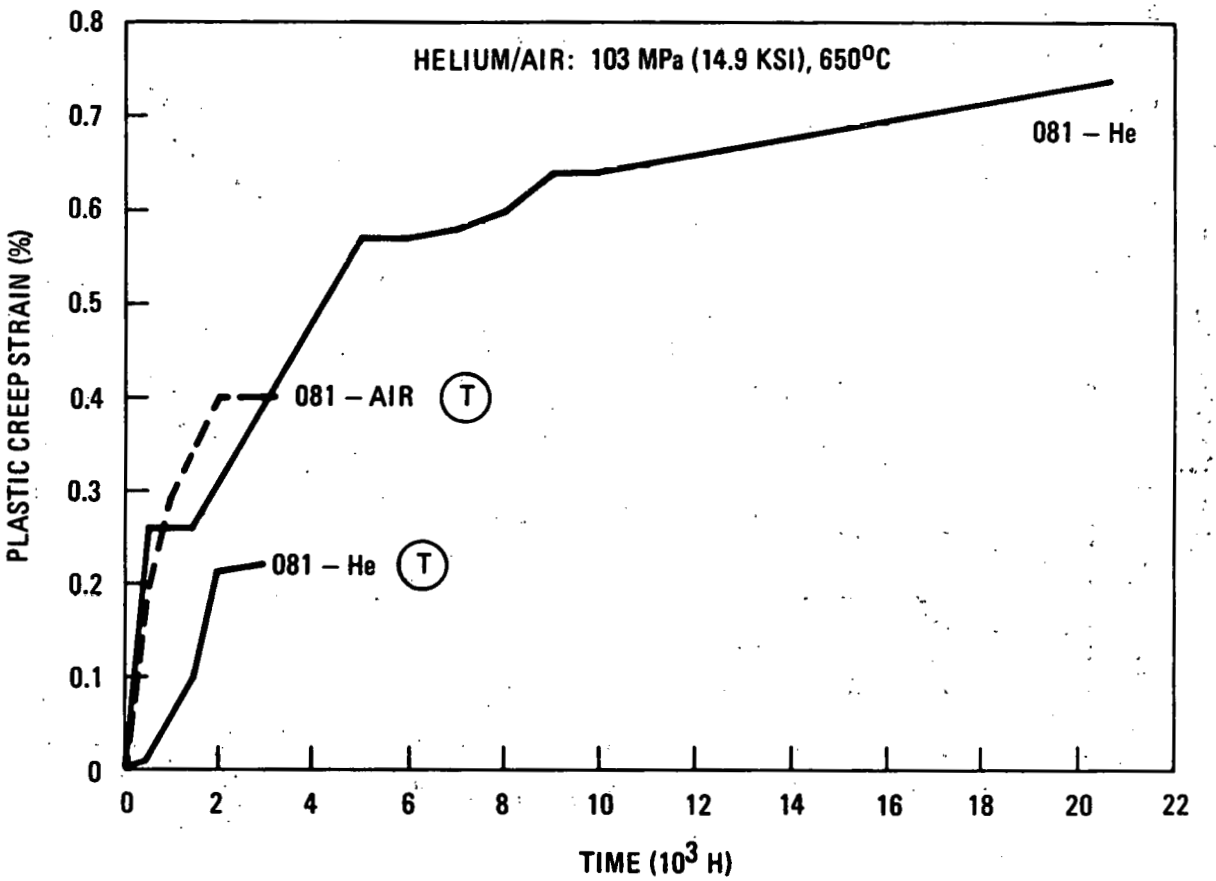

Fig. 3. Creep curves for Hastelloy X (heat 081) in air and controlled-impurity helium at 650°C (T = terminated)

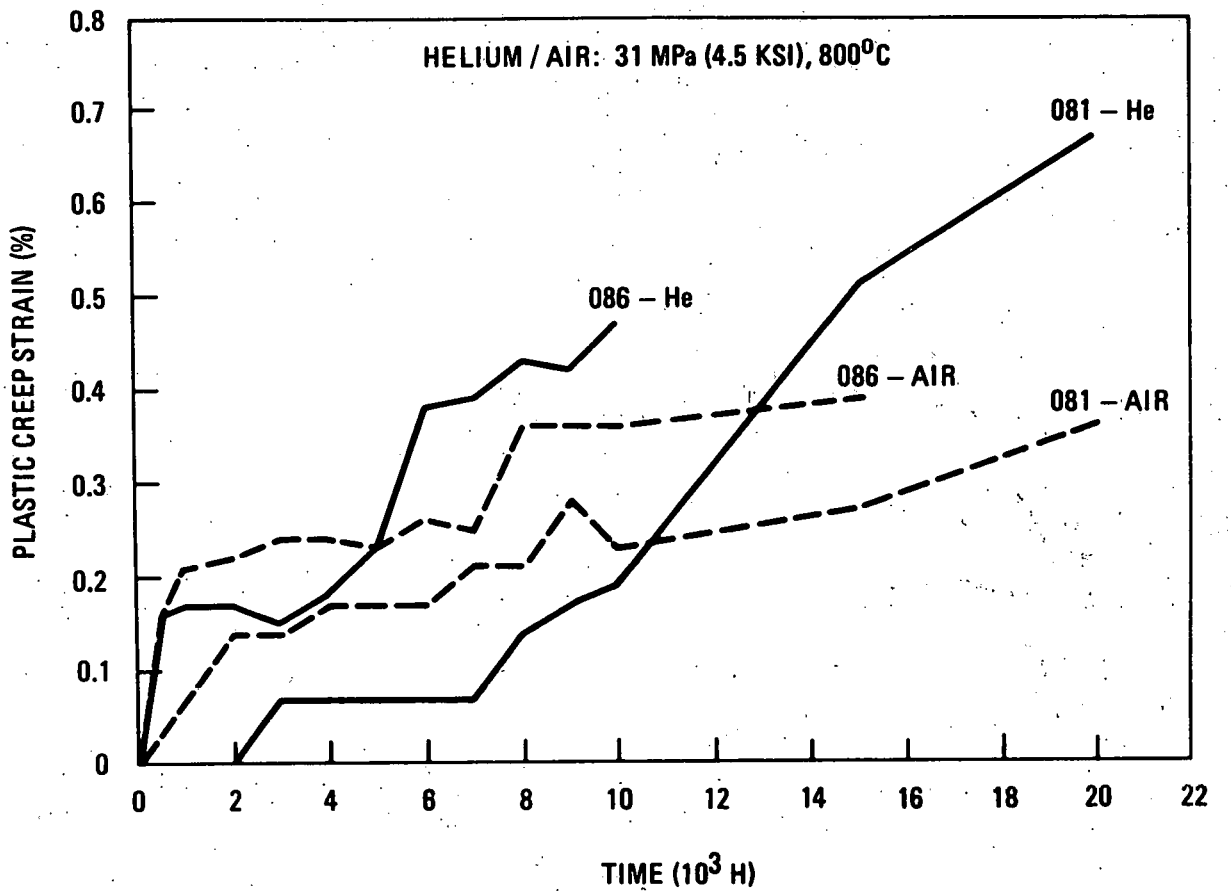

Fig. 4. Creep curves for Hastelloy X (heats 081 and 086) in air and controlled-impurity helium at 800°C

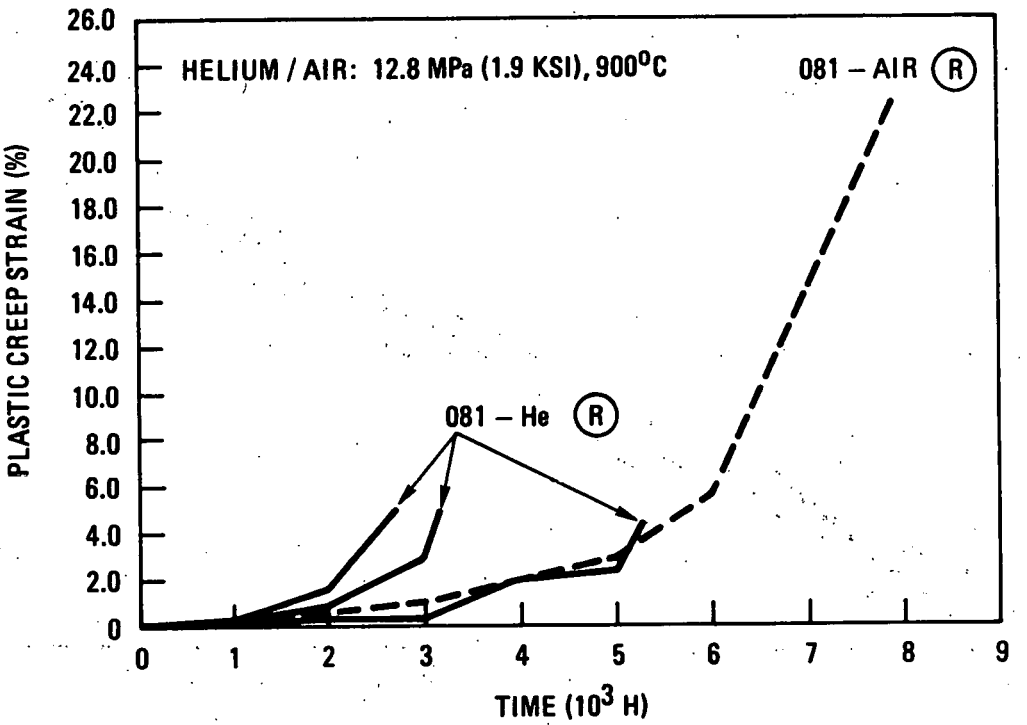

Fig. 5. Creep curves for Hastelloy X (heat 081) in air and controlled-impurity helium at 900°C (R = ruptured)

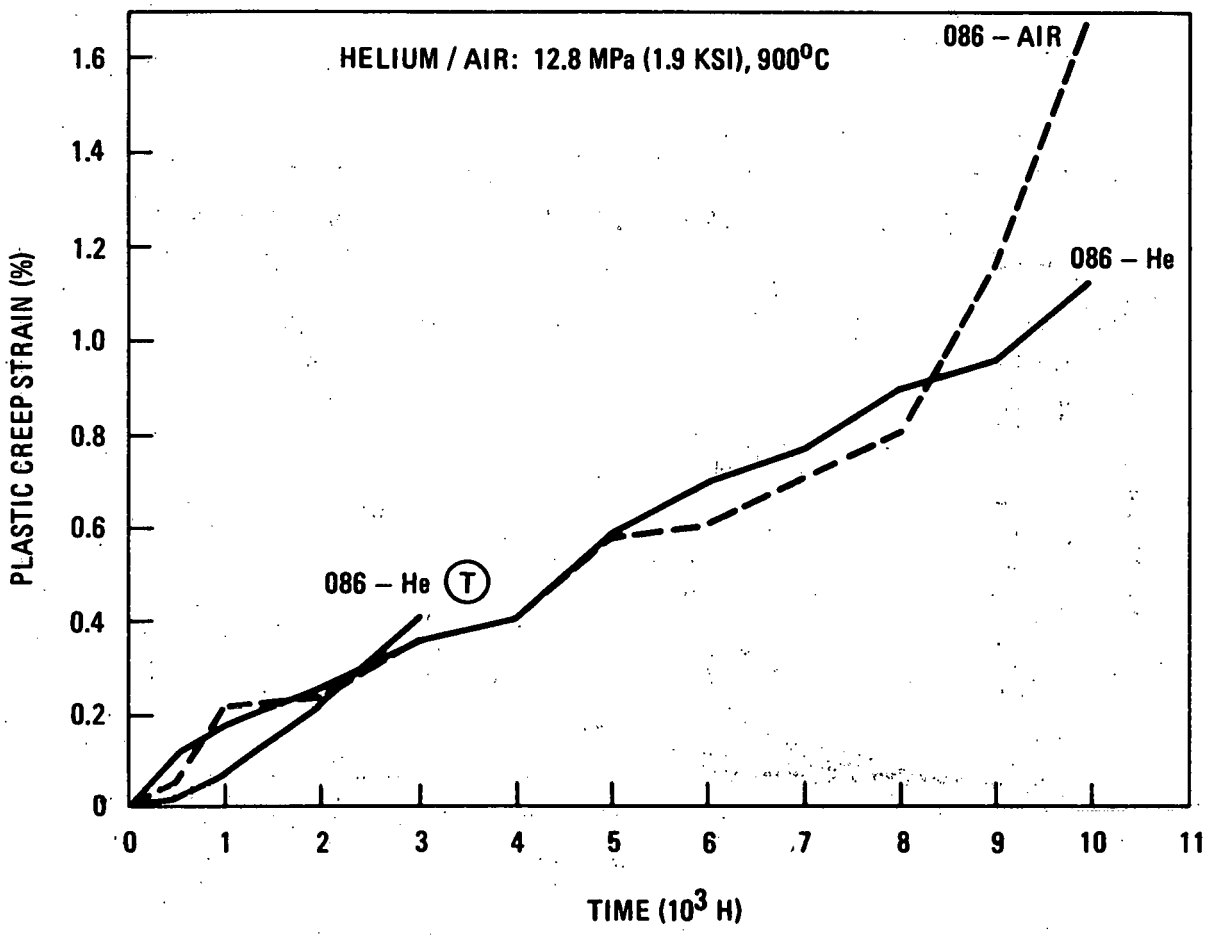

Fig. 6. Creep curves for Hastelloy X (heat 086) in air and controlled-impurity helium at 900°C (T = terminated)

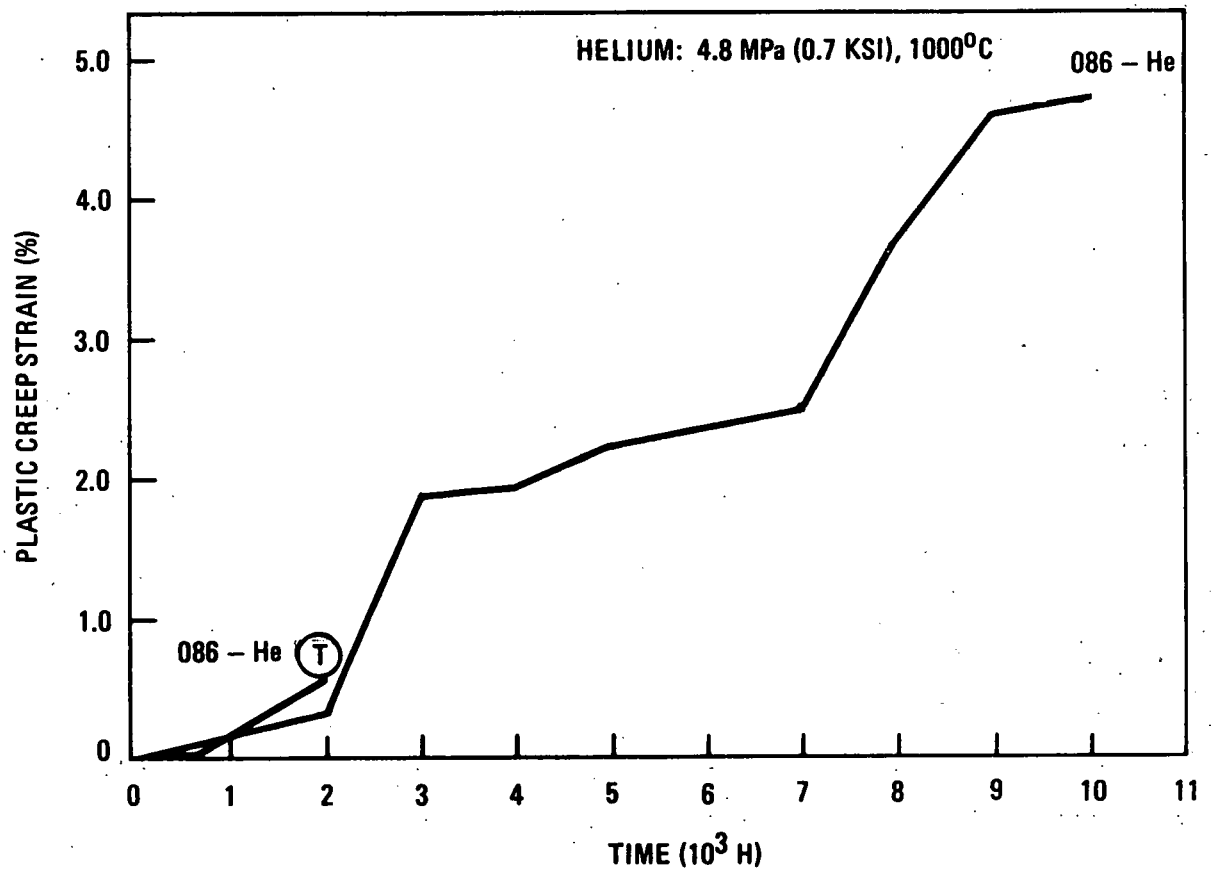

Fig. 7. Creep curves for Hastelloy X (heat 086) in controlled-impurity helium at 1000°C (T = terminated)

to the air-tested specimen for times up to ~5000 hr. The creep behavior in helium and air for heat 081 at 900°C appears to be similar during the early stages of creep (up to ~2000 hr) but deviates significantly at longer times. However, the creep data for both environments suggest that all of the test specimens experienced accelerating increases in strain at later times, which is characteristic of tertiary creep (a stage of high-temperature creep generally associated with complex phenomena, including creep deformation under increasing complex stresses, intergranular void formation, crack nucleation, and crack growth). It is not uncommon for creep curves for multiple specimens tested under identical conditions to differ markedly during third-stage creep because of the rather inhomogeneous nature of the complex processes that can occur. The low-ductility rupture of the three specimens tested in helium should be noted, however. The three specimens ruptured with 4.4 to 5.0% final plastic strain, while the same material tested in air at 900°C ruptured with ~23% final plastic strain. This heat of Hastelloy X appears to be below average in creep strength, but the data clearly show a significantly lower rupture ductility in controlled-impurity helium. The reason for the apparent low strength of this heat in comparison with the other heat of Hastelloy X is not clear, but it is suspected that the smaller grain size of the former may be a contributing factor, since fine-grained materials are generally weaker in high-temperature creep than coarse-grained materials (Ref. 4).

3.2. ROOM-TEMPERATURE TENSILE AND IMPACT PROPERTIES

3.2.1. Tensile Properties

The room-temperature tensile test results for specimens exposed unstresed and/or stressed (in creep) for 3000 h in impure helium and air are presented in Table 4. A comparison of data for helium- and air-aged specimens is presented in Fig. 8. Results obtained for solution-annealed specimens are also included. The room-temperature tensile properties presented include 0.2% offset yield strength, ultimate tensile strength, and plastic strain to failure (percent total elongation).

TABLE 4
ROOM-TEMPERATURE TENSILE TEST RESULTS FOR HELIUM- AND AIR-EXPOSED HASTELLOY X TENSILE AND CREEP SPECIMENS

Heat No.	Type of Specimen	Exposure Temp (°C)	Exposure Environment	0.2% Yield Strength (MPa)	Ultimate Tensile Strength (MPa)	Elongation (% in 25.4 mm)
081 (Solution annealed)	Tensile	--	--	465.4	799.8	42.0
086 (Solution annealed)	Tensile	--	--	329.6	776.4	46.8
081	Tensile	800	He	446.1	910.1	13.2
081	Tensile	800	Air	445.4	923.9	15.9
086	Tensile	800	He	362.0	852.2	16.1
086	Tensile	800	Air	322.7	850.2	22.0
081	Tensile	900	He	335.1	670.9	10.4
081	Tensile	900	Air	328.9	718.5	16.3
086	Tensile	900	He	272.4	626.1	12.8
086	Tensile	900	Air	275.8	726.7	23.1
081	Creep	650	He	706.7	1154.2	13.8
081	Creep	650	Air	734.3	1185.3	10.3
086	Creep	800	He	369.6	756.4	8.0
086	Creep	900	He	287.5	593.7	11.8
086	Creep	1000	He	331.7	585.4	12.0

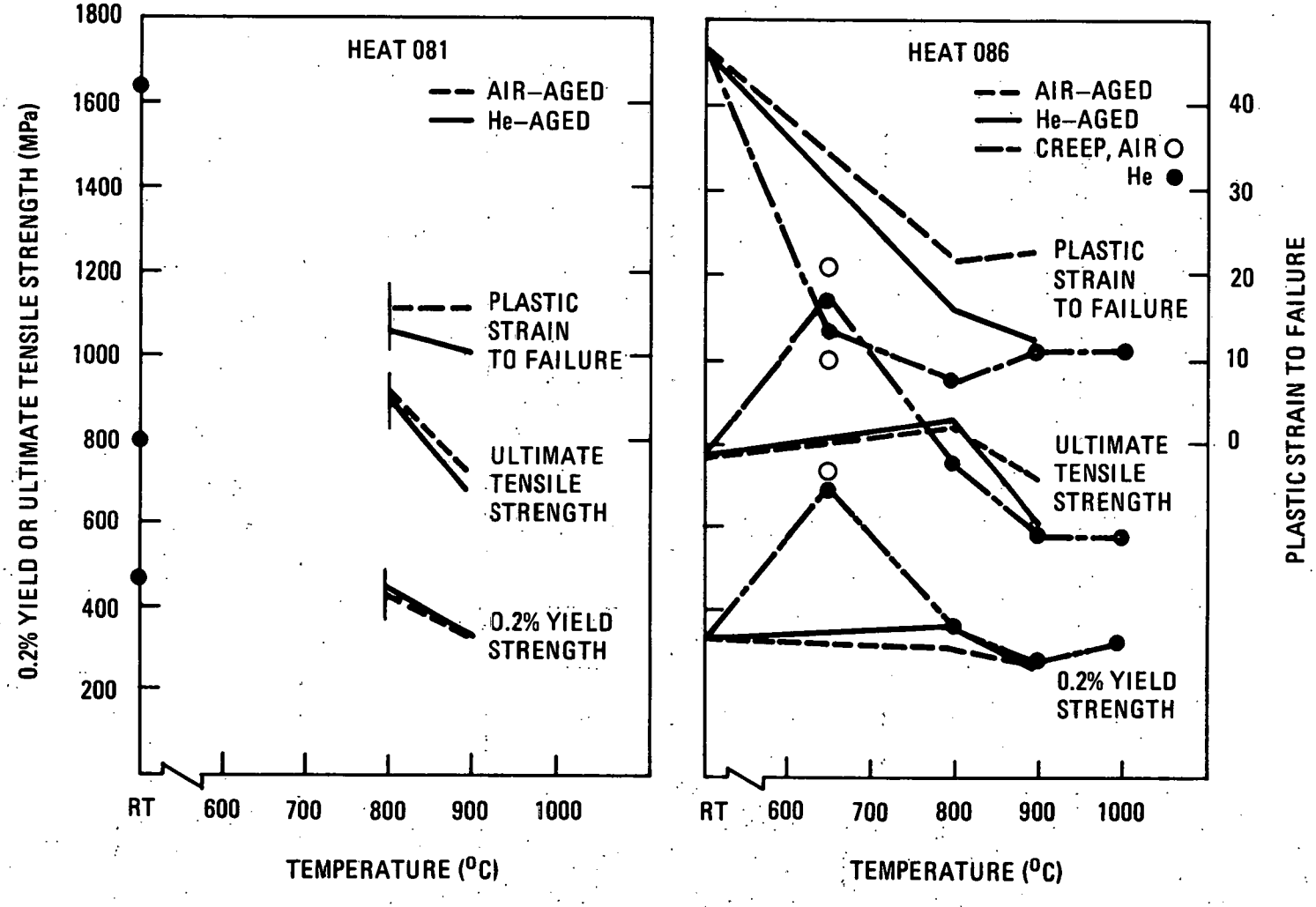

Fig. 8. Comparison of room temperature tensile properties for Hastelloy X aged stressed (creep) and unstressed in controlled-impurity helium and air for 3000 h

In the as-received (solution-annealed) condition, both heats exhibited intermediate yield strength, high ultimate strength, and substantial plastic strain to failure (ductility). The ultimate strengths and ductilities for both heats were similar, while the yield strength was significantly higher for the fine-grained heat of material (081). Unstressed aging in helium or air at 800°C resulted in only slight changes in yield strengths for both heats, compared to as-received values, significant (10 to 16%) increases in ultimate strength, and large decreases in ductilities (50 to 70% reduction relative to initial values). Yield and ultimate strengths and ductilities for both heats decreased below as-received values after unstressed aging in helium or air at 900°C. Ductilities obtained after unstressed aging at 900°C were similar to or slightly lower than values obtained after 800°C aging.

Strength values for 800°C air- and helium-aged specimens were comparable for both heats, while plastic strains to failure were slightly lower after aging in helium than in air. Yield strengths for both heats aged unstressed at 900°C were comparable in air and helium, while ultimate strength and ductility values were lower after aging in helium than in air.

Creep testing in helium of heat 086 at 800° and 900°C resulted in significant differences in residual tensile properties relative to values for unstressed specimens only at 800°C. Although yield strength values for both unstressed and stressed (crept) specimens were nearly the same, ultimate strengths and ductilities were appreciably lower for specimens crept in helium at 800°C compared to their unstressed and helium-aged counterparts. Tensile properties obtained after 900°C aging were comparable for unstressed and stressed specimens. At 650°C, no significant differences in tensile properties were observed between specimens crept in helium and air. Residual properties of 1000°C-crept specimens were comparable to those obtained after 900°C creep.

3.2.2. Impact Properties

The room-temperature impact test results for specimens exposed 3000 h in helium and air are presented in Table 5. Results are also included for as-received (solution-annealed) specimens. In the solution-annealed condition, heat 086, by virtue of its coarser grain structure, exhibited a much higher impact energy (187.4 J) than the finer-grained heat 081 specimen (62.4 J). Helium and/or air aging at 800° and 900°C substantially reduced the impact energies of both heats. Impact energies after helium aging at 800°C were lower for the fine-grained heat (081) compared to the coarse-grained material, while values for both heats were comparable after helium aging at 900°C. Impact values for heat 086 after aging at 800° and 900°C were comparable for helium- and air-aged specimens.

3.3. SURFACE AND INTERNAL MICROSTRUCTURAL CHANGES

Significant changes occurred in the surface and internal microstructures of both heats after exposure to controlled-impurity helium at 650° to 1000°C. The changes were manifestations of both thermal aging phenomena and interactions of the materials with the gaseous impurities in the helium environments.

3.3.1. Thermal Aging Effects

Internal microstructural changes, independent of the helium impurity/metal interactions which occurred, were observed in all of the helium-exposed specimens and were the result of well-known thermal aging phenomena. These same microstructural changes were also observed in air-aged specimens.

The internal microstructures of both Hastelloy X heats prior to exposure are shown in Fig. 9. Heat 086 exhibited a relatively large grain size (0.160 mm grain diameter) and contained a high density of annealing

TABLE 5
ROOM-TEMPERATURE IMPACT TEST RESULTS FOR HELIUM- AND AIR-EXPOSED HASTELLOY X CHARPY V-NOTCH SPECIMENS

Heat No.	Exposure Temp (°C)	Exposure Environment	Energy Absorbed (J)
081 (Solution annealed)	--	--	62.4
086 (Solution annealed)	--	--	187.4
081	800	He	5.3
086	800	He	9.7
086	800	He	10.6
086	800	Air	9.3
081	900	He	17.0
086	900	He	19.2
086	900	Air	15.0

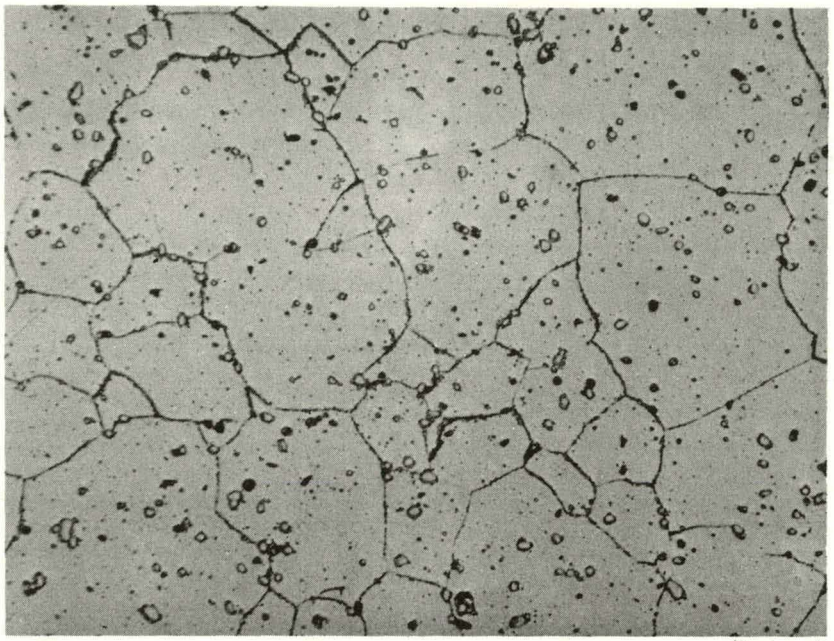

Fig. 9. Optical photomicrographs showing etched internal microstructures of Hastelloy X in solution-annealed condition. Typical phases present include coarse and fine M_6C-type carbides. Electrolytic oxalic acid etch

twins, while heat 081 exhibited a smaller grain size (0.090 mm grain diameter), a lower annealing twin density, and more distinct grain boundaries than observed for heat 086. Both solution-annealed heats contained a mixture of fine and coarse carbides dispersed in a nickel-rich austenite (γ) matrix. Large and small globular or roughly spherical carbides appeared both intra- and intergranularly throughout the microstructures. Finer and much less extensive carbides appeared within the microstructures, both intergranularly and surrounding the large globular carbides. The morphology and distribution of these carbides are characteristic of the primary molybdenum-rich M_6C-type carbides generally found in solution-annealed Hastelloy X (Refs. 5-7). Small intra- and intergranular cubic precipitates (typical of carbonitrides) were also observed occasionally in the microstructures.

Except for some differences associated with twin boundaries in the two heats, thermal aging produced similar microstructural changes for both materials during exposure. Photomicrographs shown in Figs. 10 through 13 are representative of the internal (center of specimen) microstructures of both heats after a 3000-h exposure to controlled-impurity helium or air at 650° (heat 081 only), 800°, 900°, and 1000°C (heat 086 only).

The effect of thermal aging at all temperatures was to produce additional carbide precipitation. The size, density, and locations of the precipitates relative to other microstructural features (i.e., grain and twin boundaries, etc.) in the materials varied with the exposure temperature.

Aging at 650° and 800°C generally produced precipitation of fine, discrete carbides, intra- and intergranularly, on twin boundaries, and around the much coarser primary M_6C-type carbides. At 650°C, the precipitated carbides were very fine and their density was greatest near grain boundaries and primary carbides, while at 800°C, the precipitated carbides were more uniformly distributed throughout the microstructure and were

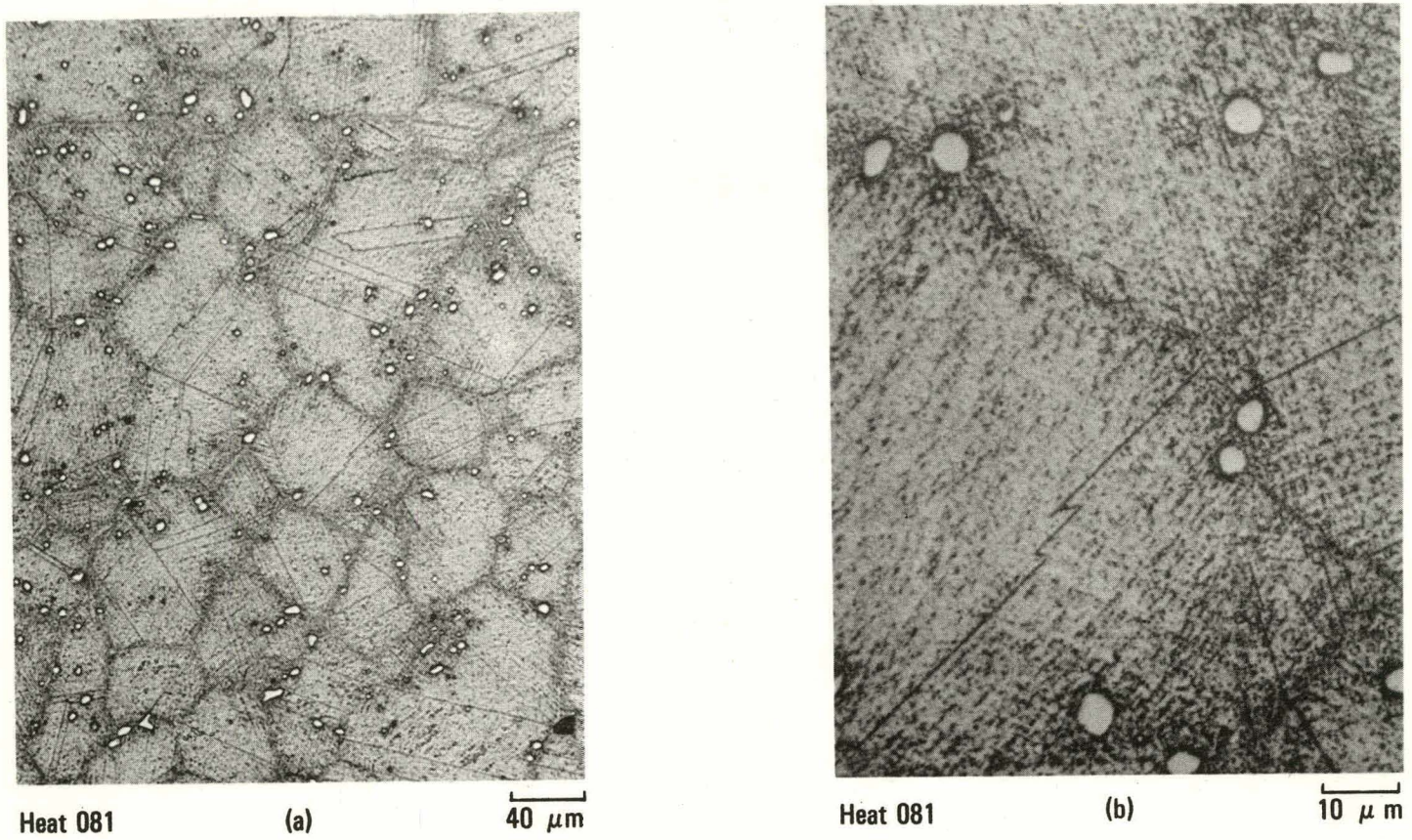

Fig. 10. Optical photomicrographs showing etched internal microstructure of Hastelloy X (heat 081) after 3000 h of thermal aging at 650°C. Electrolytic oxalic acid etch.

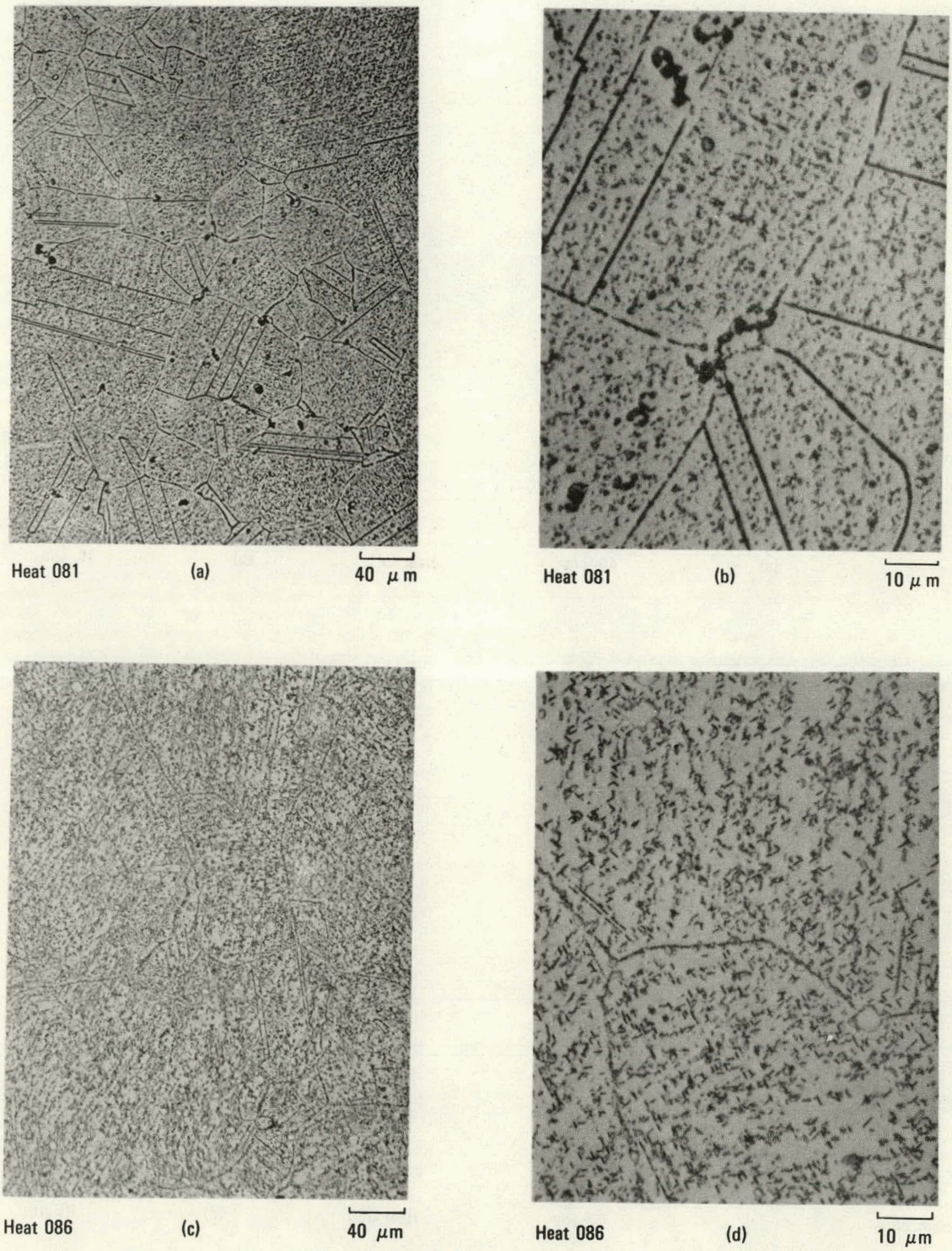

Fig. 11. Optical photomicrographs showing etched internal microstructure of Hastelloy X after 3000 h of thermal aging at 800°C. Electrolytic oxalic acid etch.

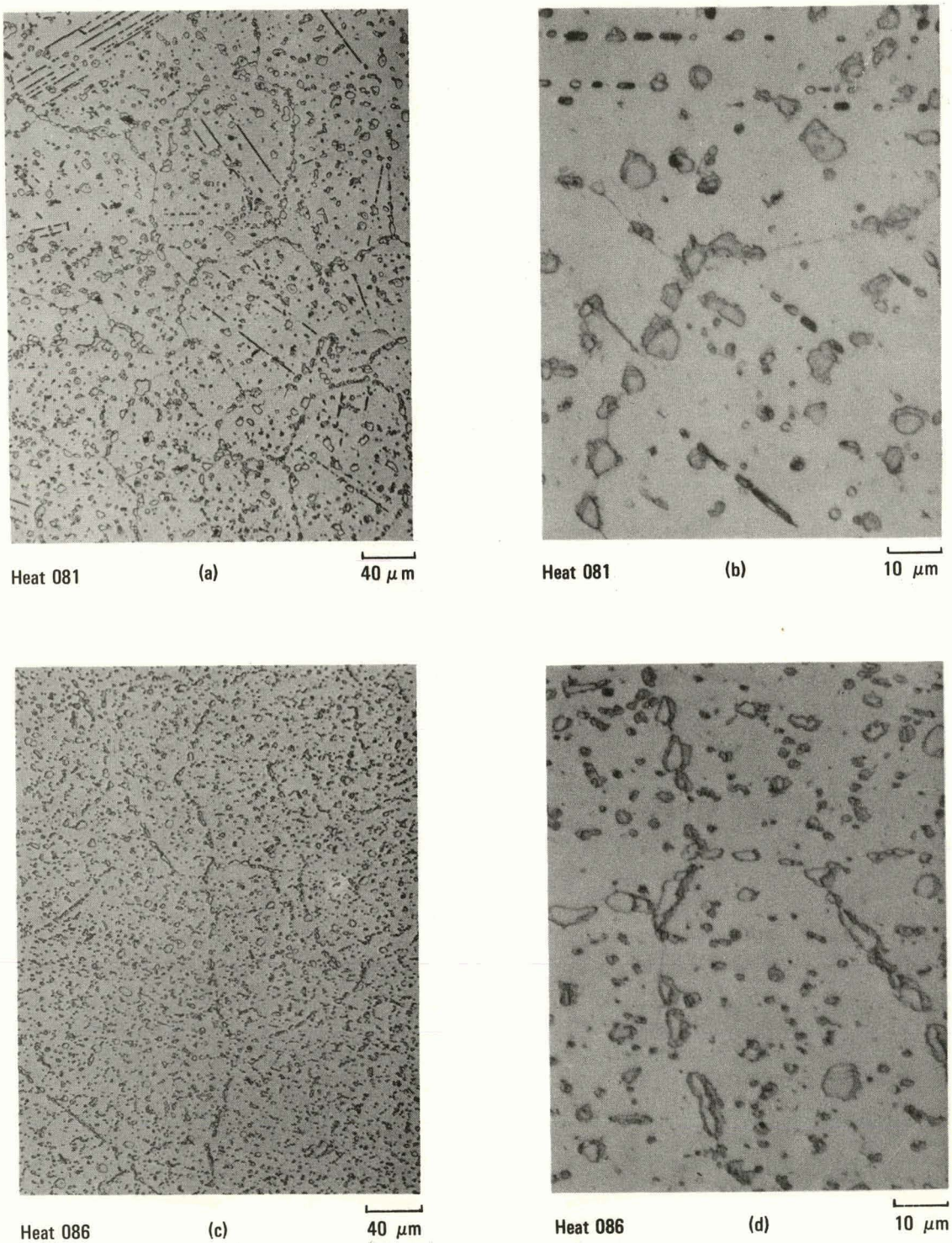

Fig. 12. Optical photomicrographs showing etched internal microstructures of Hastelloy X after 3000 h of thermal aging at 900°C. Electrolytic oxalic acid etch.

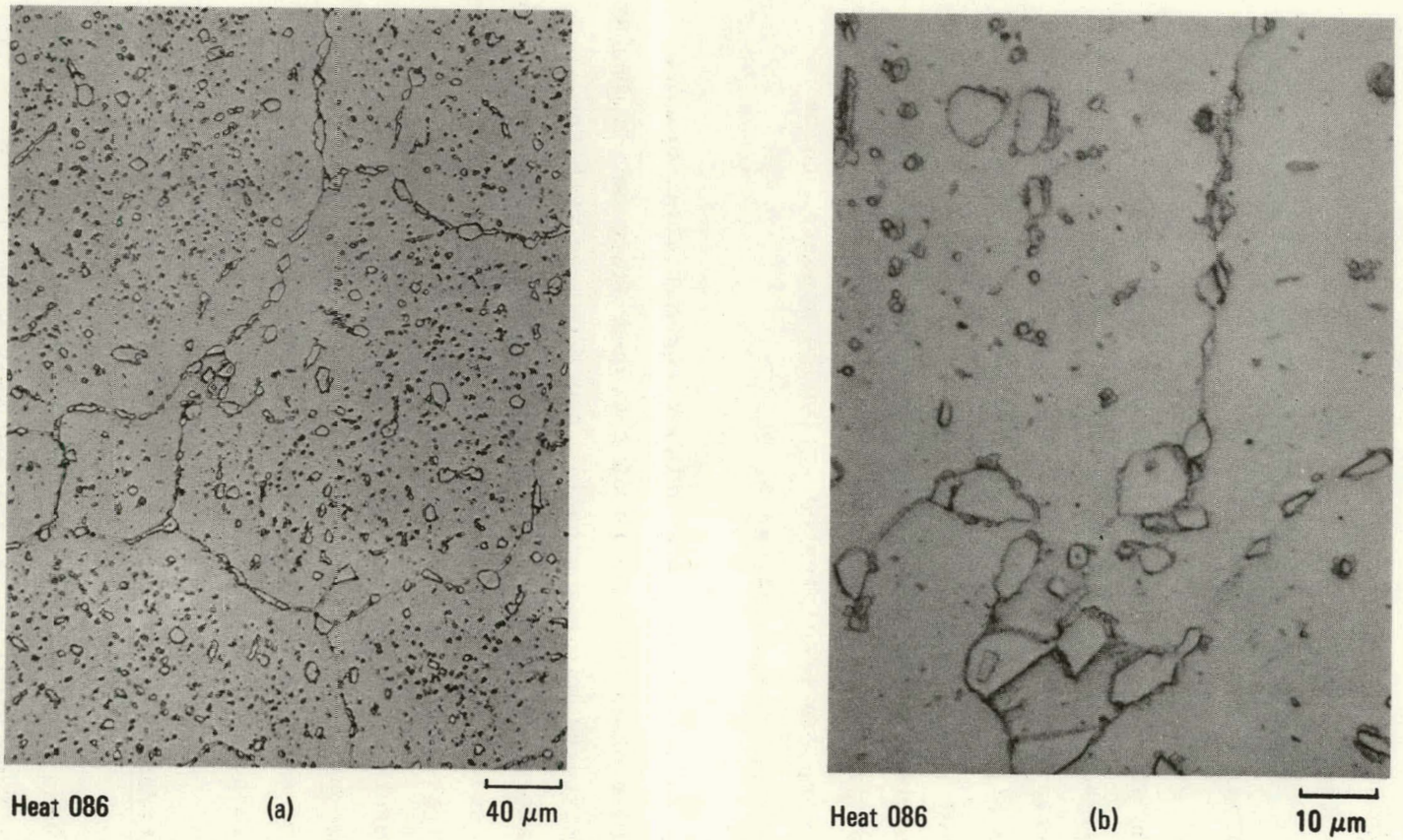

Fig. 13. Optical photomicrographs showing etched internal microstructure of Hastelloy X (heat 086) after 3000 h of thermal aging at 1000°C. Electrolytic oxalic acid etch.

slightly coarser in appearance. Twin boundary precipitation appeared to be more pronounced in the smaller-grained heat (081) of material. In addition, carbide denuded zones adjacent to grain and twin boundaries were observed after 800°C aging of both heats.

The effect of thermal aging at 900° and 1000°C was to produce a coarser distribution of precipitated carbides than that observed at the lower temperatures. An increased number of large, globular intra- and intergranular carbides, similar to the M_6C-type carbides found in the solution-annealed materials, were observed after aging at both temperatures. In addition, a distribution of intermediate and fine precipitated carbides was observed at grain and twin boundaries and within the grains of both materials. As observed at 800°C, more pronounced twin boundary precipitation was noted for heat 081 after 900°C exposure compared to heat 086. In general, the carbides precipitated at 1000°C appeared to be coarser and less dense than those observed at 900°C.

Based on the results of previous Hastelloy X thermal aging studies (Refs. 6,7), the carbides observed in both of the aged heats can be tentatively identified as mixtures of predominantly two M_6C-type carbides. Analyses of residues extracted from solution-annealed and aged Hastelloy X have indicated that a single M_6C-type carbide is predominant in solution-annealed material, while two carbides, M_6C and M_6C', are predominant in material aged at temperatures >538°C. These analyses have also indicated that M_6C' is the major phase precipitated during thermal aging at such temperatures, but the presence of σ and μ phases, especially at higher temperatures and for longer aging times, was also confirmed.

3.3.2. Helium Impurity/Metal Interactions

Interactions between the specimens and impurities in the controlled-impurity helium environment occurred at all exposure temperatures, resulting in surface oxide and carbide formation, internal oxidation,

alloying element depletion, and high-density carbide precipitation (carburization) extending into the matrix. Because of these environmentally induced reactions, both materials exhibited varying degrees of surface discoloration and scale formation, as well as increases in carbon content. The materials progressed from uniform black scales (at 650°C) to uniform gray scales with increasing temperature.

The scale morphologies of the specimens exposed to controlled-impurity helium for 300 h at temperatures from 650° to 1000°C are shown in Fig. 14. At each temperature, the scale morphologies observed for both heats were similar.

At 650°C, the surface scale observed was a very thin (~1 μm) continuous layer which was determined by SEM energy dispersive x-ray analysis (EDX) to be predominantly chromium-rich oxide. Below this thin scale, a very shallow (~10 μm) chromium-depleted region was observed.

At exposure temperatures of 800°C and higher, duplex-layered surface scales were observed consisting of an outer light-etching (white) scale and a dark appearing (gray) inner scale. At 800°C, the outer white layer appeared discontinuous and thin, while at 900°C, this white layer was generally thicker and more continuous. At 1000°C, the outer white scale was relatively thick but exhibited a tendency to spall. The outer white layer at all three temperatures was found to be a chromium-rich carbide containing small amounts of Mo, Ni, Fe, and Si, while the inner gray layer was identified as a chromium-rich oxide at 800°C and a chromium- and manganese-rich oxide (possibly spinel) at 900° and 1000°C. Beneath the duplex surface scales on the specimens exposed at 800°, 900°, and 1000°C, a denuded region appeared, depleted in those elements present in the surface scales. Within this alloy-depleted region, fine particulate internal oxides, primarily aluminum- and silicon-rich, were observed. In general, the thickness of the alloy-depleted region and the depth of internal oxidation increased with increasing exposure temperature. No internal oxidation was observed for the 650°C-exposed specimen.

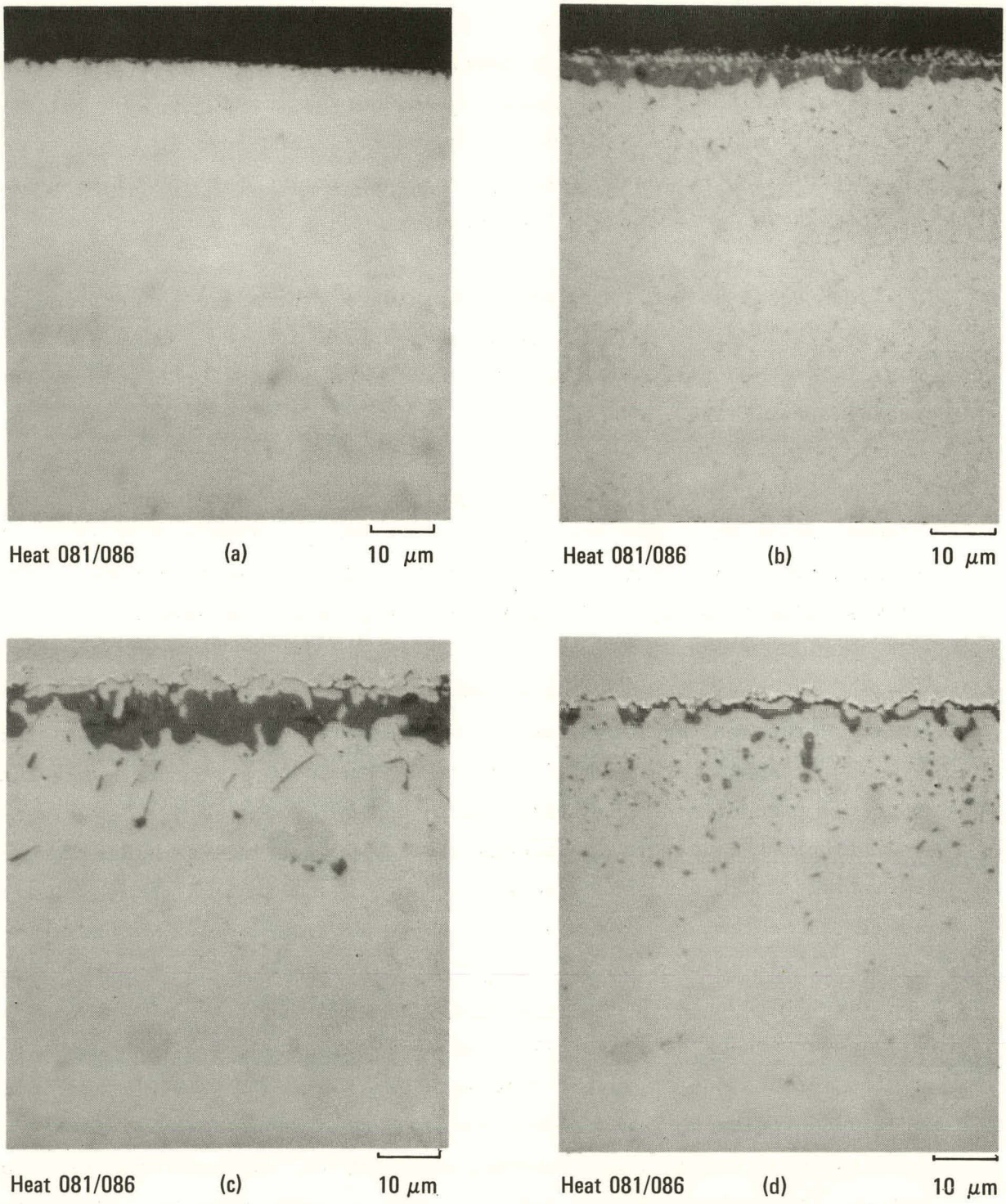

Fig. 14. Optical photomicrographs showing surface condition and unetched subsurface microstructure of Hastelloy X after 3000-h exposure in controlled-impurity helium at (a) 650°C, (b) 800°C, (c) 900°C, and (d) 1000°C. Scale morphologies and subsurface microstructures shown are typical of both heats of material employed in study. White layer shown above scale in (c) and (d) is electrodeposited nickel.

Carburization was observed for both of the Hastelloy X heats at temperatures greater than 650°C. The carburization appeared as a near-surface zone of high-density precipitated carbides and resulted in increases in the bulk carbon content of the materials. The precipitated carbides were observed intra- and intergranularly, and often at twin boundaries. The grain boundary and twin boundary precipitated carbides also appeared thicker and more continuous nearest the surface. Optical photomicrographs which are representative of the carburization observed for both heats at each temperature are shown in Figs. 15 and 16. These photomicrographs were obtained by the differential interference contrast (DIC) method using an optical microscope with polarized light. Under these conditions, the precipitated carbides resulting from carburization appeared to stand in relief relative to the other caribdes present in the microstructure, possibly because of their different hardnesses. Because of this effect, these precipitated carbides were relatively easy to locate during subsequent scanning electron microscopy examinations and were readily identified as chromium-rich carbides by EDX analysis. Other carbides (not in relief) present in the microstructures were found to be primarily molybdenum-rich (presumably M_6C-type).

Depths of carburization for each specimen cross section were determined optically using the DIC method. The carburization depths for each specimen exposed in controlled-impurity helium are presented in Table 2 and are plotted as a function of exposure temperature in Fig. 17. The values indicated represent the average of eight measurements around the cross section of each specimen. At 650°C, no evidence of carburization was observed. For higher temperatures, carburization depths increased with increasing exposure temperature.

In general, within experimental scatter, specimens from differect heats exhibited similar depths of carburization at each exposure temperature, although larger variations in carburization depth were observed for the large-grained heat (086), especially at 900°C. At 800° and 900°C, the creep specimens, which were exposed to controlled-impurity helium under an

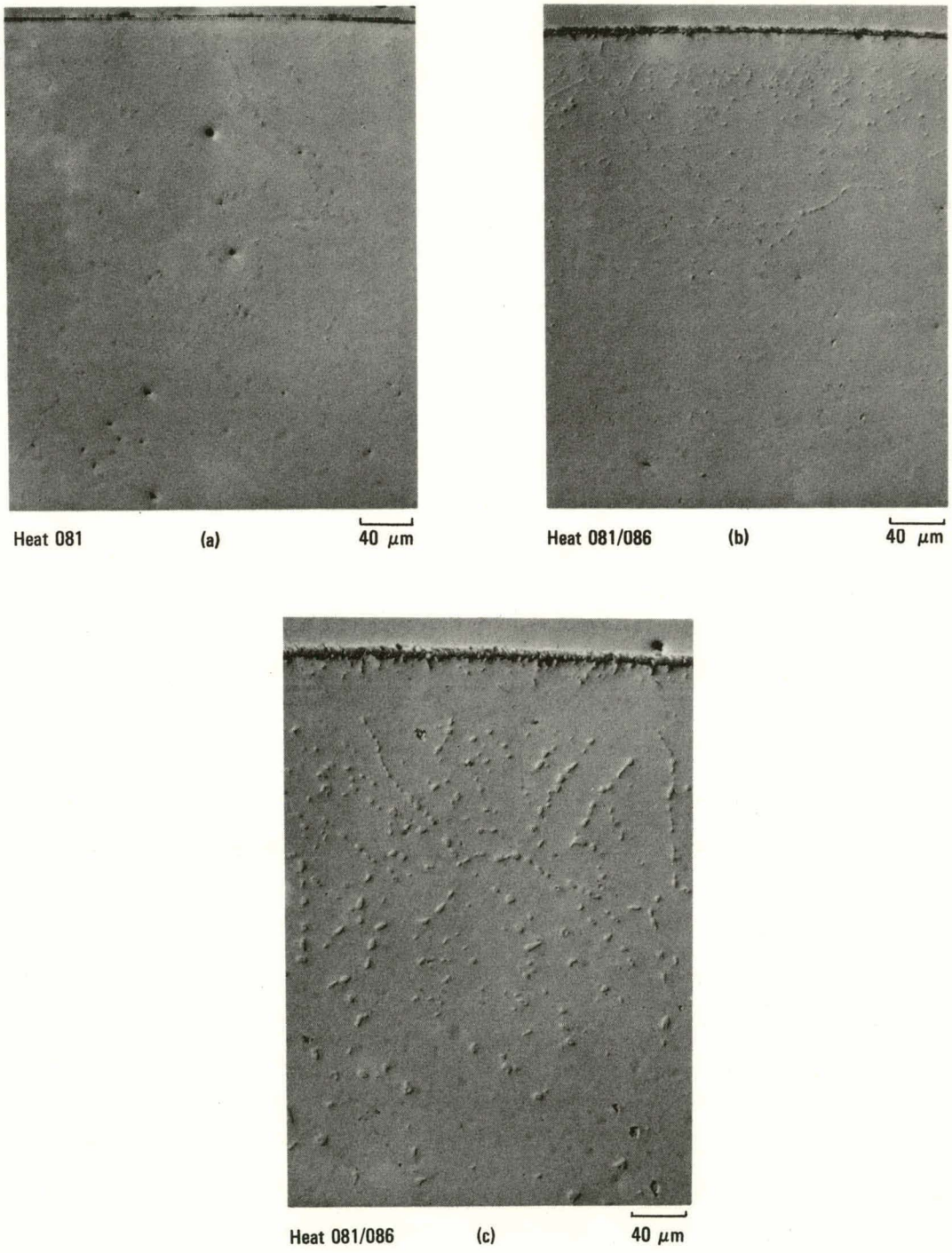

Fig. 15. Optical photomicrographs showing unetched near-surface microstructure of Hastelloy X after 3000-h exposure in controlled-impurity helium at (a) 650°C, (b) 800°C, and (c) 900°C. Microstructures in (b) and (c) show increased carbide precipitation (carburization) near surface and are typical of both heats of material used in study. White layer above surface scale is electrodeposited nickel.

Fig. 16. Optical photomicrograph showing unetched near-surface microstructure of Hastelloy X (heat 086) after 3000-h exposure in controlled-impurity helium at 1000°C. Microstructure shows increased carbide precipitation (carburization) near surface. White layer above surface scale is electrodeposited nickel.

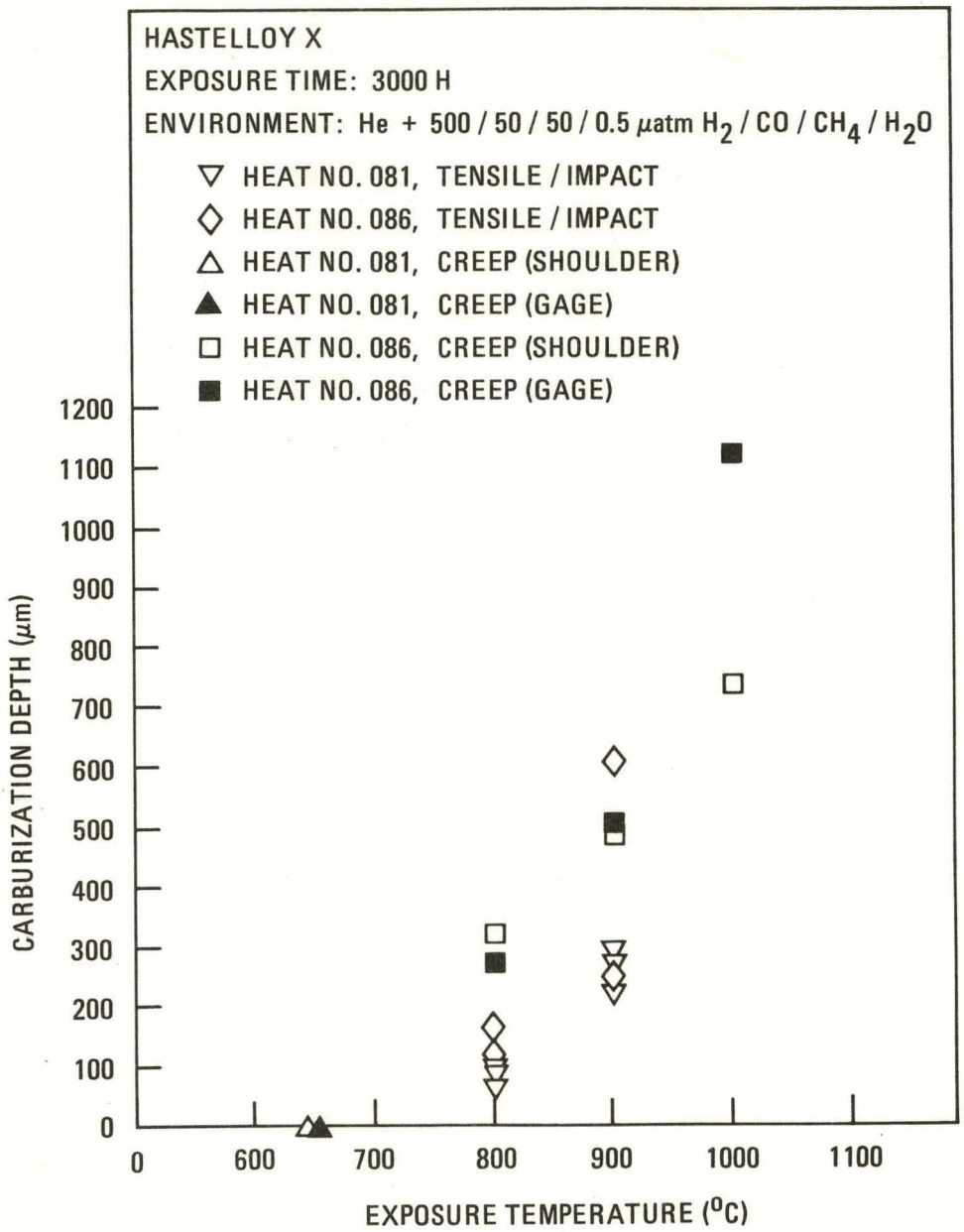

Fig. 17. Carburization depth as a function of exposure temperature for Hastelloy X exposed unstressed and stressed (creep) for 3000 h in controlled-impurity helium

applied stress, exhibited carburization depths similar to those obtained for unstressed tensile and impact specimens. No significant differences in carburization depth were observed between values obtained in stressed (gage section) and unstressed (shoulder section) regions of the creep specimens at 800° and 900°C. At 1000°C, however, stressed areas of the creep specimen exhibited substantially greater depths of carburization than unstressed areas.

Bulk carbon analyses were also performed on cross-sectional slices of the 3000-h helium-exposed specimens. The values obtained for each specimen are also presented in Table 2. The 650°C-exposed (creep) specimen exhibited only a slight increase in bulk carbon content, from 0.092 wt % in the solution-annealed condition to 0.10 wt % after exposure, a relative increase of 8.7%. Significant differences in carbon content between as-received and exposed specimens were observed at 800°, 900°, and 1000°C. Carbon levels generally tended to increase with increasing exposure temperature for both heats and were somewhat greater at each exposure temperature for the finer-grained heat (081). Values of bulk carbon content obtained were slightly larger for stressed (creep) specimens of heat 086 at 800°C compared to unstressed specimens but were within the range of values obtained on unstressed specimens at 900°C.

3.3.3. X-Ray Phase Analysis

Electrolytic extractions for x-ray diffraction phase analysis were carried out at room temperature for specimens exposed in helium and air at 900°C. Four successive extractions were conducted, corresponding to material removal at different depths from the specimen surface. In each extraction, a layer approximately 50 μm thick was removed from the specimen surface. The precipitate phases extracted at different depths from the helium- and air-exposed specimens were identified by x-ray diffraction and are listed in Table 6 along with the relative amounts obtained. The first layer extractions from the helium-exposed specimen contained oxide, oxide spinel, and M_6C- and $M_{23}C_6$-type carbides, while the air-exposed

TABLE 6
X-RAY DIFFRACTION ANALYSIS RESULTS OF PRECIPITATE PHASES EXTRACTED FROM HASTELLOY X AFTER 3000-H EXPOSURE TO CONTROLLED-IMPURITY HELIUM AND AIR AT 900°C

Phases Present	Approximate Depth of Extraction From Surface (μm)							
	Helium Exposure				Air Exposure			
	50	100	150	200	50	100	150	200
Cr_2O_3	Major	Minor	--	--	Major	Medium	Minor	--
Oxide spinel	Medium	Minor	--	--	Minor	Minor	--	--
M_6C a_o = 10.96 Å and 10.94 Å	Minor	Major	Major	Major	--	Minor	Medium	Major
M_6C' a_o = 10.87 Å	--	--	Minor	Minor	Minor	Major	Major	Major
$M_{23}C_6$ a_o = 10.69 Å	Minor	Minor	Medium	Medium	--	--	--	--
μ phase a_o = 4.747 Å C_o = 25.64 Å	--	--	Minor	Minor	--	Minor	Minor	Medium

specimen contained oxide, oxide spinel, and M_6C-type carbides. No $M_{23}C_6$ carbide phase was observed in the air-exposed specimen. Inside the specimens (third and fourth extractions), oxide and oxide spinel were not observed for either helium- or air-exposed conditions. The air-aged specimen primarily contained two M_6C-type carbides and a small amount of phase, while the helium-exposed specimen contained large fractions of M_6C (a_o = 10.96 Å) and $M_{23}C_6$ carbides and minor amounts of μ phase and another M_6C carbide (a_o = 10.87 Å).

In helium-exposed specimens, the increase in carbon concentration near the exposed surface, i.e., carbon availability for precipitation reactions, results in the precipitation of $M_{23}C_6$ carbides relative to M_6C-type carbides. The $M_{23}C_6$ carbides are chromium-rich and presumably chromium is readily available in air-aged as well as helium-aged specimens. Therefore, as the bulk carbon concentration increases, the favored carbide precipitation reaction becomes the formation of $M_{23}C_6$. The precipitation of $M_{23}C_6$-type carbides has also been observed in air-aged specimens exposed at 538°C after long exposure times in a different experiment (Ref. 8). In this latter case, the sluggish nature of molybdenum diffusion at 538°C kinetically inhibits M_6C' precipitation whereby the formation of chromium-rich $M_{23}C_6$ is possible.

4. DISCUSSION

To accurately take into account the effects of oxidation and carburization in simulated HTGR helium environments on the mechanical properties of Hastelloy Alloy X, it is necessary to be familiar with microstructural changes which accompany thermal exposure at elevated temperatures. Assessments of thermal instability and associated mechanical property evaluations for Hastelloy X have been reported (Refs. 6-9). Long-term thermal aging studies have shown that precipitation reactions have a marked effect on the mechanical properties, particularly the higher strain rate tests, e.g., Charpy V-notch impact properties (Refs. 6,7).

The predominant thermal aging reaction for Hastelloy X is the precipitation of a M_6C carbide variant, for which the specific lattice parameter changes with temperature, presumably related to changes in elemental constituent mobilities (Refs. 6,7). At lower exposure temperatures, $M_{23}C_6$ has been observed (Refs. 9,10). At higher temperatures, μ and σ phases can precipitate; however, their characteristic morphologies are such that they have little effect on the mechanical properties (Refs. 6,7). Carbide precipitation reactions leading to the formation of M_6C along grain boundaries and in some cases twin boundaries are believed to control the impact properties of thermally aged specimens. In cases where a continuous grain-boundary network of carbides can be formed, fracture modes change from ductile rupture to a mixed mode consisting of ductile microvoid coalescence combined with inter- and transgranular cleavage. This type of behavior is associated with lower temperature exposures. At higher temperatures, the carbides tend to coalesce, resulting in a much coarser distribution and only a marginal effect on mechanical behavior.

In the two heats studied in the present investigation, similar microstructural changes occurred with thermal aging, as mentioned previously.

The primary difference observed in the aging response/microstructure of the two heats was the increase in twin-boundary carbide precipitation in the fine-grained heat (081). For this heat, the twins appeared to be decorated to a greater extent than those of the larger-grained heat, despite the fact that the twin density was higher in the latter heat of material.

Exposure in the simulated reactor helium environment containing 500 μatm H_2/50 μatm CH_4/50 μatm CO/~1 μatm H_2O produced carburization at temperatures of 800° to 1000°C. This carburization was manifested not only in an increase in bulk carbon concentration but also an increase in carbide precipitation. As the carbon concentration increased, $M_{23}C_6$ carbides formed with increasing ease, and the enhanced precipitation of $M_{23}C_6$ along grain and twin boundaries and M_6C/matrix interfaces dominated any other microstructural changes occurring via the carburization.

At 650°C, no carburization was observed; therefore, very little change was noted between properties of air-exposed and helium-exposed specimens. All property changes between the as-received and exposed specimens resulted primarily from the thermal aging reactions and were not related to the exposure in controlled-impurity helium.

The impact toughness properties (presented in Table 5) indicate a marked effect of grain size on the as-received Charpy V-notch impact toughness value. An increase in grain size from 0.090 mm to 0.160 mm resulted in a tripling of the impact toughness. Aging in controlled-impurity helium and air at 800° and 900°C resulted in decreases in impact toughness but showed virtually no variation between helium and air exposures. At 800°C, where carbide precipitation was finer, and where more continuous networks of carbides along grain and twin boundaries were formed, impact toughness was lowered to approximately 10 J. At 900°C, agglomeration of carbides occurred and impact toughness values following exposure were somewhat higher, i.e., 15 to 20 J. Figure 18 shows the fracture surfaces at the base of the notch in the Charpy V-notch specimens. For both heats,

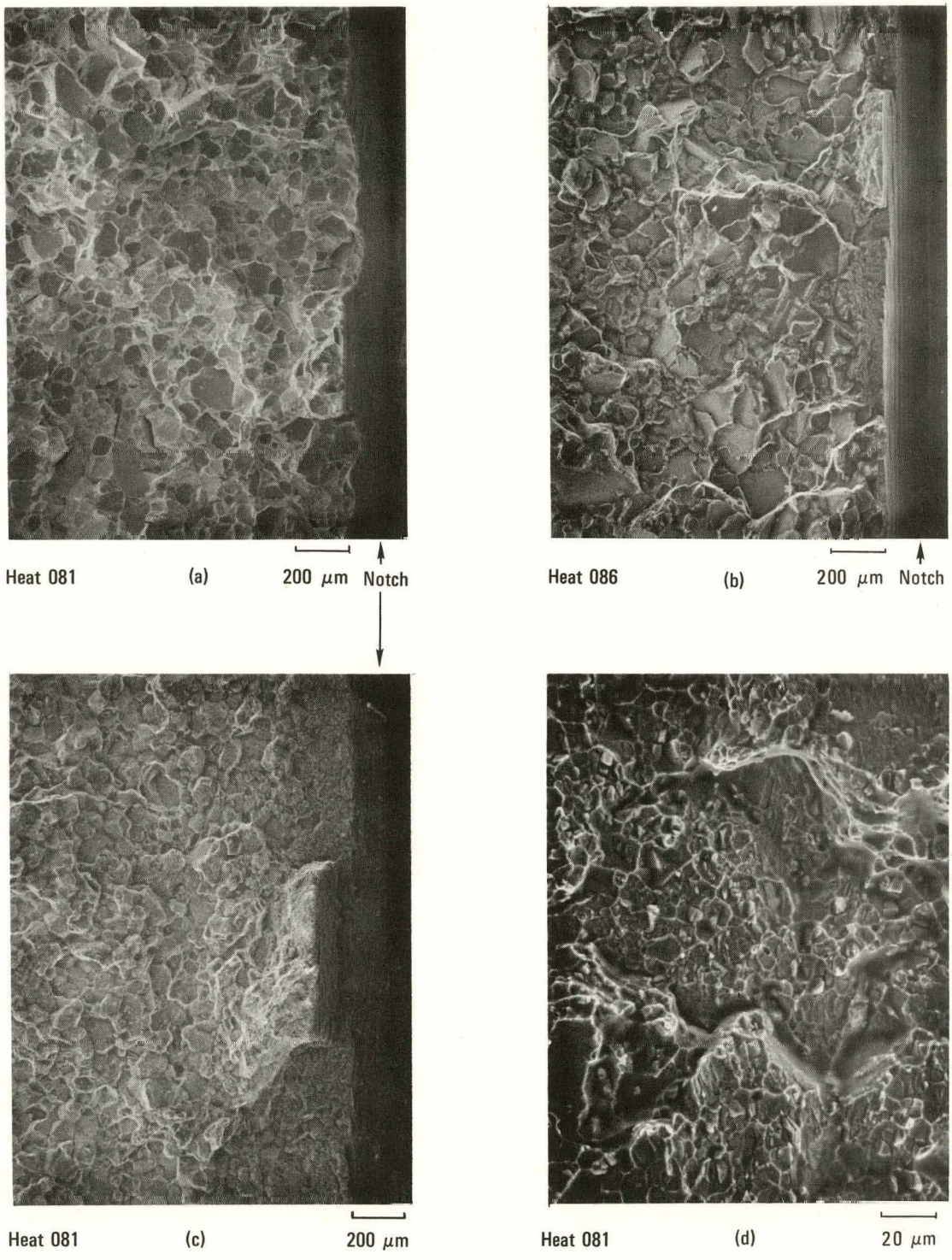

Fig. 18. SEM fractographs showing fracture surfaces near V-notch of Hastelloy X impact toughness specimens tested after exposure in controlled-impurity helium: (a) heat 081, 800°C; (b) heat 086, 800°C; (c) and (d) heat 081, 900°C

the failure mechanism indicated after exposure at 800°C [Fig. 18(a),(b)] was a combination of inter- and transgranular cleavage. After 900°C exposure, the crack propagation mode was predominantly intergranular, where grain boundaries have separated with evidence of some microvoid coalescence [Fig. 18(c)], thus accounting for the increase in toughness above that for 800°C exposures. A higher magnification fractograph [Fig. 18(d)] shows the tendency for intergranular carbides to cleave. Also shown are regions of ductile material adjacent to the carbides which plastically deform and therefore increase energy absorption capability. The fracture behavior can be explained in terms of the thermal aging effects (Refs. 6, 7,9) with little effect of exposure to simulated reactor helium observed.

The grain size difference also explains the yield strength variation observed in the as-received condition. Heat 081, with the smaller grain size, had the higher yield strength, as would be expected. The decreases in both ultimate tensile strength and total elongation values following exposures in helium or air at 800° and 900°C were similar for both heats and can again be associated with the carbide precipitation morphologies. The interfaces between carbides and matrix or grain (twin) boundary material are inherently weak and can separate, forming voids. In addition, if the applied stress becomes high enough, the carbides can cleave, which also forms a void. The effect of helium exposure, compared to thermal aging in air, on the mechanical properties of both heats was more pronounced for those specimens exposed under stress. At 800°C, in helium, the values of ultimate tensile strength and total elongation were slightly lower for the specimen that was stressed during exposure.

There was a dramatic difference in tensile fracture mode, however, between the two heats of material. Figure 19 shows the fracture surfaces observed for the tensile tests. Comparison of the fracture behavior for heat 081 [Fig. 19(a),(b),(c)] with that for heat 086 [Fig. 19(d),(e),(f)] points out the major differences. In heat 081, where twin-boundary carbide precipitation seemed to be accentuated, there was a tendency toward

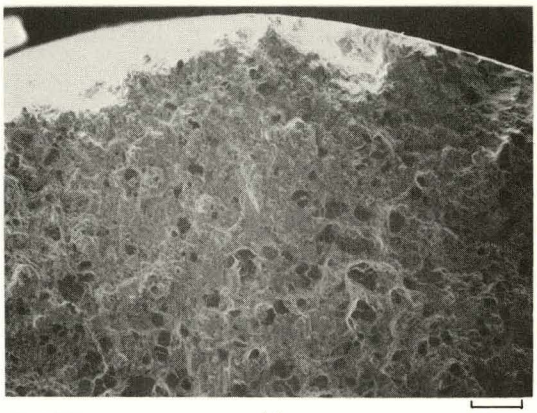

Heat 081 (a) 200 μm

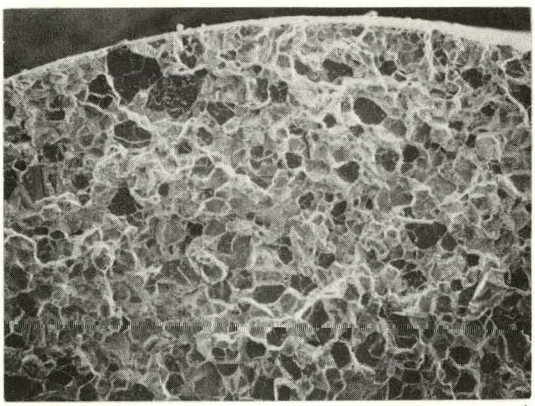

Heat 081 (b) 200 μm

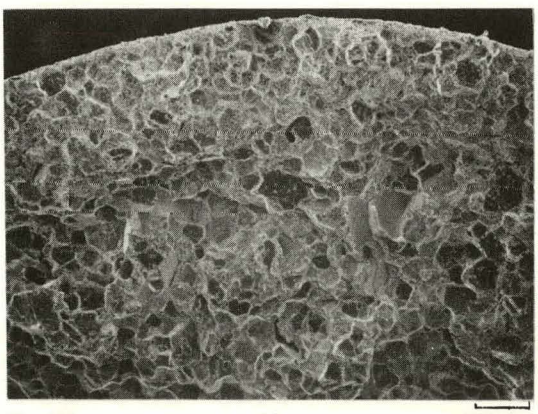

Heat 081 (c) 200 μm

Fig. 19. SEM fractographs showing typical fracture surfaces of heat 081 Hastelloy X specimens tensile tested after exposure in controlled-impurity helium at (a) 650°C, (b) 800°C, and (c) 900°C (page 1 of 2)

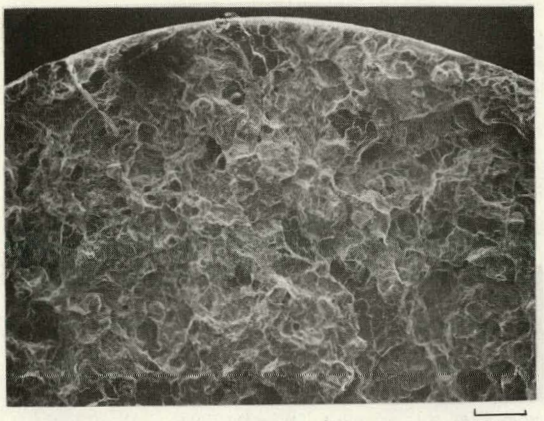

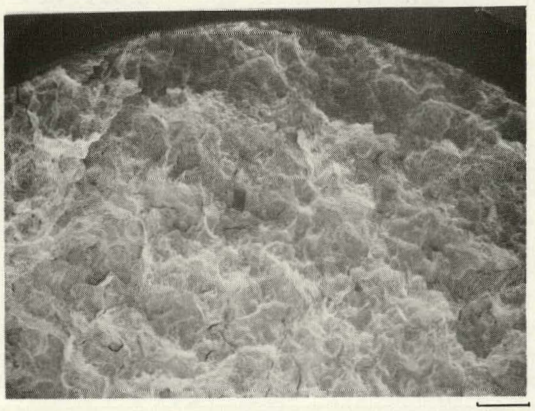

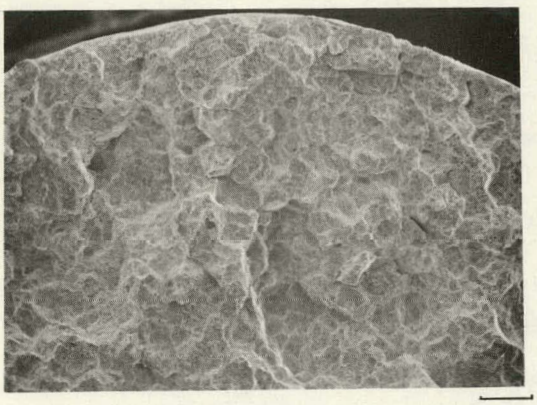

Fig. 19. SEM fractographs showing typical fracture surfaces of heat 086 Hastelloy X specimens tensile tested after exposure in controlled-impurity helium at (d) 800°C, (e) 900°C, and (f) 1000°C (page 2 of 2)

transgranular cleavage. This is shown most clearly in Fig. 19(b), representative of a specimen exposed at 800°C. The transgranular cleavage is presumably a result of continuous carbide networks along twin boundaries. In Fig. 19(d), (e), and (f), the fracture mode for heat 086 was microvoid coalescence regardless of test temperatures in the range of 800° to 1000°C. At 800°C, there is an indication that some cleavage occurred but only to a limited extent.

For heat 081, Fig. 19(c) shows a change in fracture mode from microvoid coalescence near the surface (in the carburized zone) to more cleavage in the thermally aged portion. Although not a strong effect, the increased density of coarser carbides in the carburized zone may have promoted void formation. At 650° and 800°C, no transition could be observed [Fig. 19(a) and (b)].

Figure 20 shows longitudinal cross sections near the fracture surfaces for specimens of both heats which were tensile tested after being exposed to controlled-impurity helium. For heat 081, where twin-boundary carbide precipitation occurred to a greater extent, Fig. 20(a), (b), and (c) clearly show that crack propagation occurred primarily along grain boundaries and twin boundaries. Several grains show cleavage facets along these decorated twin boundaries. Figure 20(d), (e), and (f), for heat 086, show that propagation tended to be confined to intergranular paths for this heat.

Figure 21 shows higher magnification fractographs of the 1000°C helium-exposed tensile-tested specimen. From Fig. 21, cleaved carbides and void coalescence are apparent.

Longitudinal cross sections of tensile-tested helium-exposed specimens for both heats clearly showed that for 900°C exposure, crack initiation was associated with the carburized zone of the specimen. Figure 22 shows that cracks tended to nucleate in the carburized zone and then propagate primarily along grain boundaries. Although not shown in this figure, crack propagation along twin boundaries was also common for heat 081.

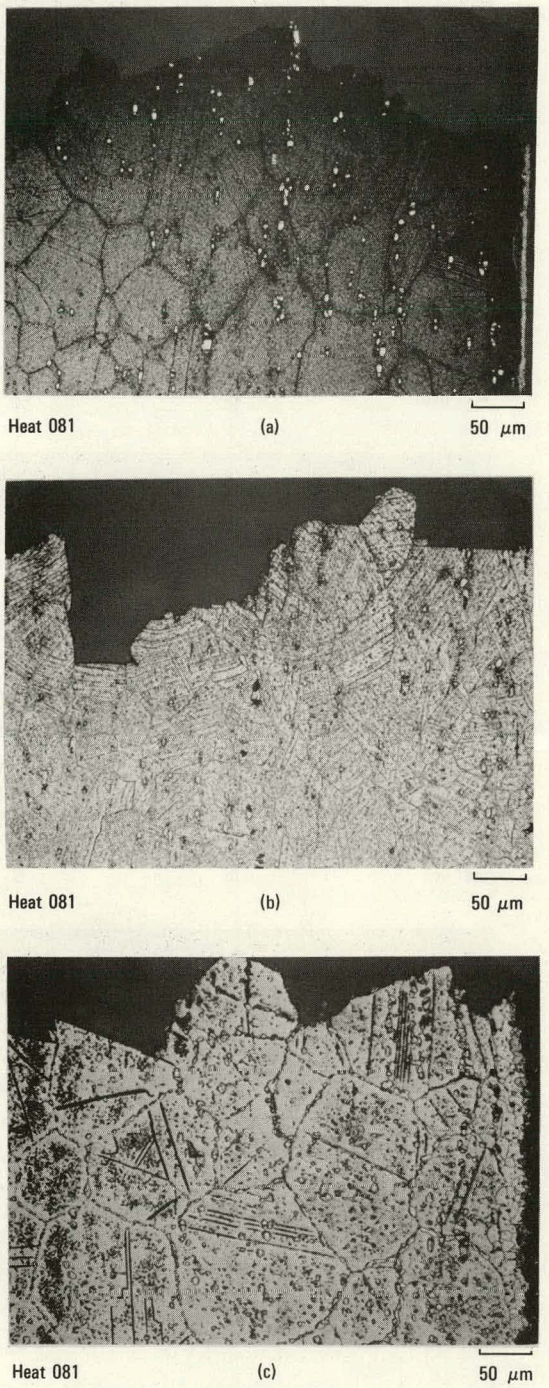

Fig. 20. Optical photomicrographs showing etched microstructures adjacent to fracture surfaces of heat 081 Hastelloy X specimens tensile tested after exposure in controlled-impurity helium at (a) 650°C, (b) 800°C, and (c) 900°C. Elcctrolytic oxalic acid etch (page 1 of 2)

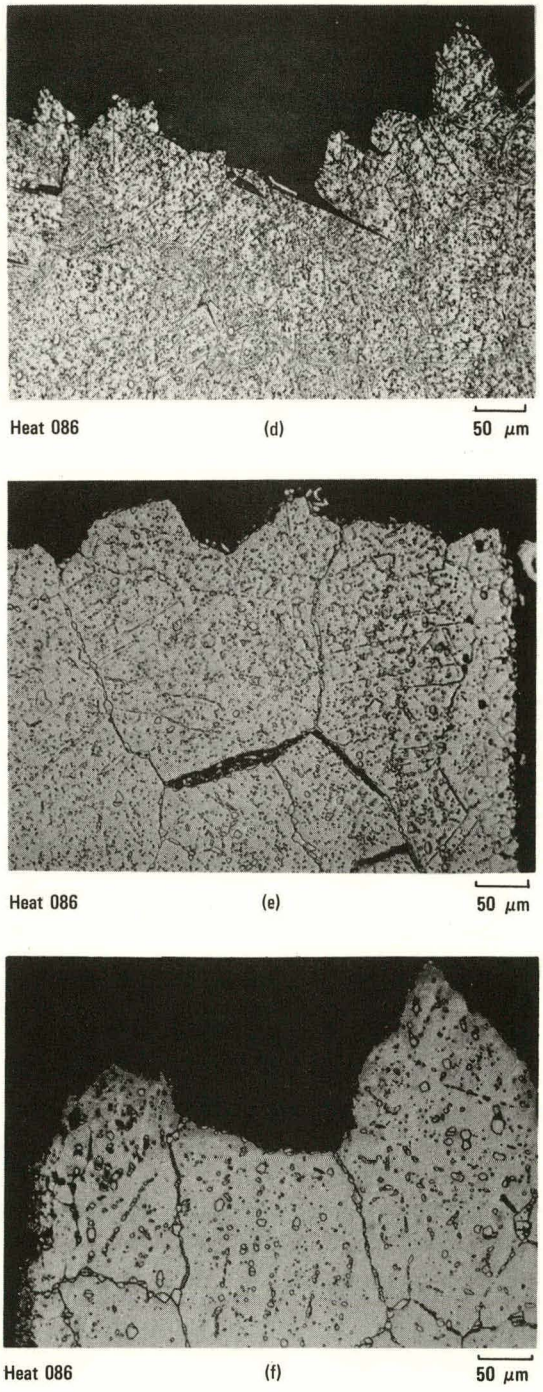

Fig. 20. Optical photomicrographs showing etched microstructures adjacent to fracture surfaces of heat 086 (Hastelloy X specimens tensile tested after exposure in controlled-impurity helium at (d) 800°C, (e) 900°C, and (f) 1000°C. Electrolytic oxalic acid etch (page 2 of 2).

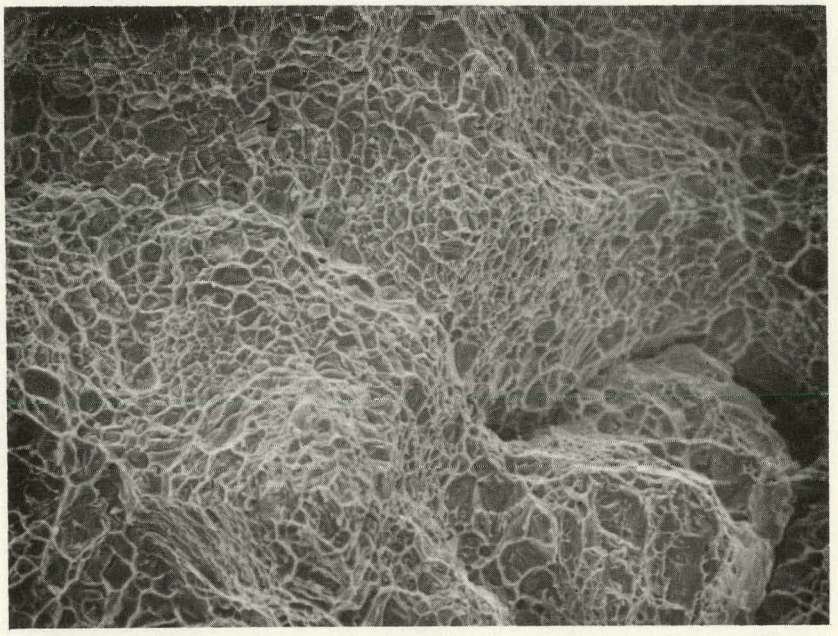

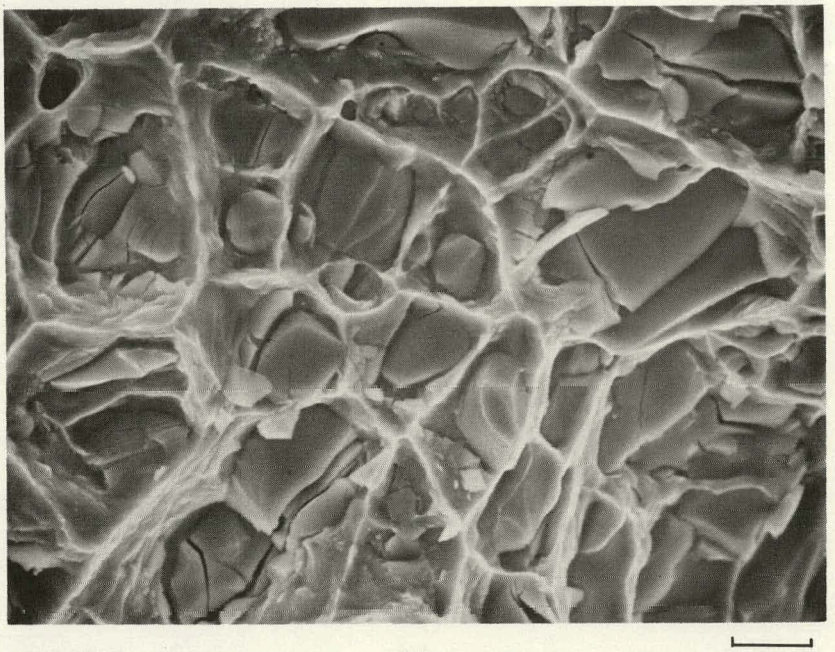

Fig. 21. SEM fractographs showing fracture surface of heat 086 Hastelloy X specimen tensile tested after controlled-impurity helium exposure at 1000°C. Fractographs illustrate microvoid coalescence and carbide cleavage resulting in void formation.

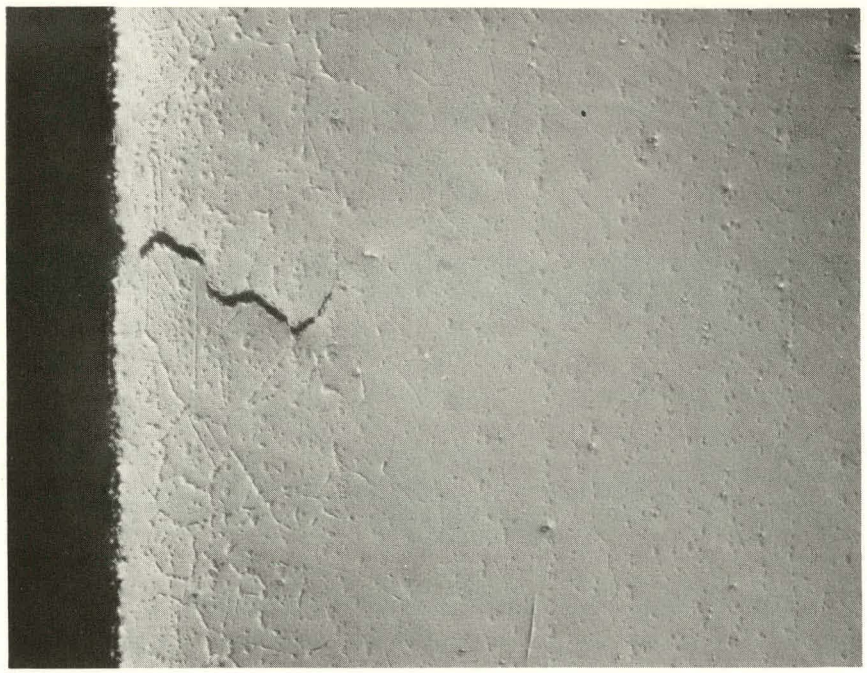

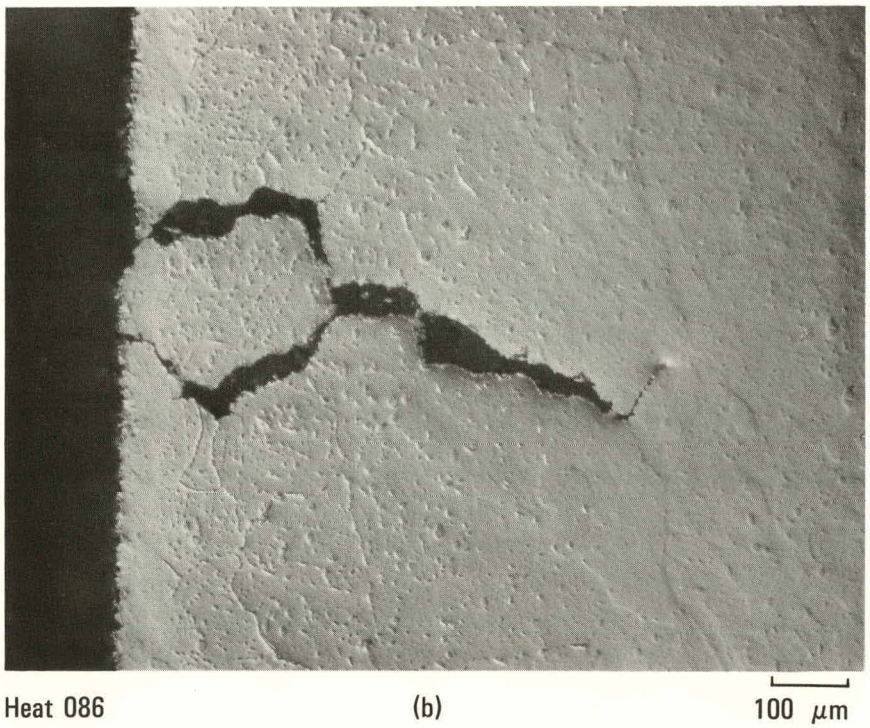

Fig. 22. Optical photomicrographs showing unetched microstructure near outside surface of Hastelloy X specimens tensile tested after controlled-impurity helium exposure at 900°C for (a) heat 081 and (b) heat 086. Photomicrographs show crack formation within carburized surface zone. DIC method.

Table 7 summarizes the microstructural observations and corresponding tensile fracture behavior for heats 081 and 086. The primary effect of long-term exposures was to decrease the ultimate tensile strength and the total elongation while having little influence on yield strength. It is important to note that in the worst cases observed there was still substantial ductility remaining, i.e., total elongation values of ~8%. The carburized zones found in helium-exposed specimens apparently act as areas of preferred crack nucleation; however, the impact of this behavior does not significantly degrade the overall tensile properties as compared to thermally aged material.

There is an indication from the creep tests that heat 081 may be a weak heat of material. Several failures (at 900°C) occurred at applied stress levels where significantly longer rupture lifetimes would have been expected. Of the four failed specimens, three were tested in helium while one was tested in air. A comparison of the rupture ductilities (total creep strain in this case) shows that the specimens tested in helium had elongation values about one-fourth that of the air specimen, i.e., 4 to 5% as compared to 23%. The weakness of heat 081 compared to heat 086 is most probably related to the smaller grain size and, therefore, greater contribution of grain-boundary sliding to crack and void nucleation. This variation can be attributed to heat-to-heat differences in alloy chemistry and processing history (i.e. fabrication and annealing treatments) and their subsequent effects on the aging response of the materials.

Total creep strains of 4 to 5% for helium-tested specimens as compared to 23% for the air-tested specimen must be considered low and may be the result of the additional carbide precipitation in the carburized zone of the specimens. The additional precipitates may tend to limit plastic flow, thereby making the carburized zone act as a constraint with respect to the elongation and plastic flow of the test specimen. From Fig. 6, it is apparent that for the air-aged specimen, the plastic flow which occurs in third-stage creep (tertiary creep) far exceeds that of any of the controlled-impurity helium specimens tested under the same conditions.

TABLE 7
SUMMARY OF MICROSTRUCTURAL AND ROOM-TEMPERATURE TENSILE TEST FRACTURE OBSERVATIONS FOR HASTELLOY X EXPOSED IN A SIMULATED REACTOR HELIUM ENVIRONMENT IN THE TEMPERATURE RANGE 650° TO 1000°C

Exposure Temp (°C)	Microstructural Observations		Fracture/Fractography Observations	
	Carburized Zone	Thermally Aged	Carburized Zone	Thermally Aged
650 (081 only)	No enhanced carbide formation	Extensive grain and twin boundary carbide precipitation; fine dispersion of matrix carbides; carbides very fine throughout	Fracture characteristics similar to those observed in thermally aged condition; no carburized zone	Mixed mode: microvoid coalescence and intergranular/transgranular cleavage
800 (081 and 086)	Surface denuded zone; fine matrix and grain boundary carbides with continuous networks observed at some boundaries	Fairly continuous network of discrete grain and twin boundary carbides (081); Widmanstatten matrix precipitates; denuded zones along grain boundaries	Fracture characteristics similar to those observed in thermally aged condition, both heats	Heat 081: mixed mode, microvoid coalescence, and intergranular/transgranular cleavage; heat 086: predominantly microvoid coalescence
900 (081 and 086)	Surface denuded zone; generally discrete carbide formation at grain boundaries and in matrix; fairly continuous networks near surface in carburized region	Large discrete carbide precipitates along grain and twin boundaries (081) and throughout matrix; even distribution	Heat 081: predominantly microvoid coalescence; heat 086: microvoid coalescence, intergranular propagation	Heat 081: mixed mode, microvoid coalescence, and intergranular/transgranular cleavage; heat 086: microvoid coalescence, intergranular propagation
1000 (086 only)	Extensive carbide precipitation at grain boundaries with decreasing tendency to form continuous networks with increasing distance from exposed surface; carbides coarser near surface	Very large, discrete carbides; fairly continuous networks along some grain boundaries	Fracture characteristics, similar to those observed in thermally aged condition	Ductile rupture; microvoid coalescence; cleavage of large carbides; voids formed at carbide/matrix, carbide/grain boundary interfaces

Another possibility is that the carburized zone acts as a preferred area for crack and void nucleation, as it does in the tensile tests. This would explain why similar behavior could be observed in the early stages of the creep test, where environmental interactions might have minimal effects, whereas in later stages, cracks nucleated in the carburized zone of the helium-exposed specimens, thus limiting their total creep elongations.

Longitudinal cross sections of the failed specimens showed a high density of voids formed uniformly across the air-tested specimen. A similar examination of the helium-tested specimens seemed to indicate that cracks were concentrated in the areas of the specimen either within or adjacent to the carburized zone. It is important to note that the poor performance in controlled-impurity helium tests was limited to the one heat of material (081) and that the other heat behaved satisfactorily.

At 650° and 800°C, the creep behavior of helium- and air-tested specimens was quite similar, indicating that for the exposure times considered there was no strong effect of the controlled-impurity helium environment. The creep behavior of heat 086 at 1000°C may have been influenced by carburization, but without companion air data no definitive conclusions can be drawn concerning impure helium effects at this temperature.

5. CONCLUSIONS

1. Carburization has been identified as the primary corrosion phenomenon, with respect to degrading mechanical properties, for Hastelloy Alloy X exposed to a simulated reactor helium environment (He/500 μatm H_2/50 μatm CO/50 μatm CH_4/~1 μatm H_2O) at temperatures of 800° to 1000°C. No carburization was observed at an exposure temperature of 650°C within the 3000 h exposure period.

2. Enhanced carbide precipitation within the carburized zone occurs by the matrix, grain-boundary, and twin-boundary precipitation of $M_{23}C_6$-type carbides. The M_6C variant, ordinarily observed as precipitating in thermally aged material, does not readily form in the carburized zone; only primary M_6C carbides are present.

3. The degree of carburization, in terms of the depth of carburization and increase in bulk carbon concentration, increases dramatically at temperatures $\geq$900°C.

4. The microstructural changes which occur with thermal aging at the various temperatures are shown to control the mechanical behavior. Strength and impact toughness properties are relatively unaffected by carburization for times up to 3000 h. Creep and tensile ductilities are decreased as a result of carburization, although substantial ductility remains in both cases. Enhanced crack and void nucleation in the carburized zone is believed responsible for the decrease in ductilities.

ACKNOWLEDGMENTS

The authors appreciate the contributions of S. S. Liang, R. B. Akin, and W. H. Hodgson, who assisted in specimen preparation, inspection, mechanical testing and analyses, and data reduction and documentation. The authors also express their thanks to D. R. Wall, who assisted in the scanning electron microscopy analyses, and to Dr. P. K. Gantzel, who assisted in the x-ray diffraction analyses. In addition, the authors wish to acknowledge S. N. Rosenwasser for helpful technical discussions and contributions in the early phases of the work.

REFERENCES

1. Rosenwasser, S. N., and W. R. Johnson, "Gas-Turbine HTGR Materials Screening Test Program Interim Results," ERDA Report GA-A13931, General Atomic Company, June 30, 1976.
2. Rosenwasser, S. N., and W. R. Johnson, "Gas-Turbine HTGR Materials Screening Test Program, Quarterly Progress Report for the Period July 1, 1976 Through September 30, 1976," ERDA Report GA-A14122, General Atomic Company, September 30, 1976.
3. Rosenwasser, S. N., and W. R. Johnson, "Gas-Turbine and Advanced HTGR Materials Screening Test Program, 10,000-Hour Results and Semiannual Progress Report for the Period Ending March 31, 1977," ERDA Report GA-A14407, General Atomic Company, July 1977.
4. Garofalo, F., Fundamentals of Creep and Creep-Rupture in Metals, The Macmillan Company, New York, 1966.
5. Sobol, G. P., and R. Stickler, "Microstructure of Ni-Based Super Alloys," Physica Status Solidi 35, 11-52 (1969).
6. Lai, G. Y., "An Investigation of the Thermal Stability of a Commercial Ni-Cr-Fe-Mo Alloy (Hastelloy Alloy X)," Metallurgical Transactions 9A, 827-831 (1978).
7. Lai, G. Y., and L. D. Thompson, "Effects of Thermal Aging on the Mechanical Properties of Ni-Cr-Mo-Fe Alloy," DOE Report GA-A15016, General Atomic Company, August 1978.
8. Thompson, L. D., General Atomic Company unpublished data, June 1978.
9. Clarke, W. L., and G. W. Titus, "Evaluation Study of Hastelloy X as a Nuclear Cladding, Volume I - Oxidation and Structural Stability Investigations," USAEC Report AGN-8289, Nuclear Division, Aerojet-General Corporation, June 1968.

GENERAL ATOMIC COMPANY
P. O. BOX 81608
SAN DIEGO, CALIFORNIA 92138